UNIVERSITY OF KWAZULU-NATAL

Tracing star formation in groups and filaments around a young active galaxy cluster at $z \sim 1.46$

by

Nondumiso Khumalo

Submitted in fulfillment of the
academic requirements for the degree of
Master of Science,
in the
School of Mathematics, Statistics, and Computer Science,
University of KwaZulu-Natal

Durban
July 2022

John 3:16

Abstract

XMMXCS J2215.9-1738 is one of the most distant spectroscopically confirmed clusters discovered in the X-ray band at a redshift $z = 1.46$. It is unusual in that it hosts a number of starburst galaxies in its core. In this project we will use optical/IR data taken from the Canada France Hawaii Telescope Legacy Survey Deep 4 (CFHTLS D4) field , along with recent MeerKAT radio observations to survey the large-scale environment around the cluster and study the environmental effects on the star formation of galaxies in groups and filaments around this cluster. This will be the first study that uses radio continnum data to calculate the SFR of J2215 since previous studies have done so using OII emission (Hayashi et al., 2010) or IR luminosities (e.g Hilton et al., 2009; Ma et al., 2015; Stach et al., 2017).

We use `EAZY` to calculate the photometric redshifts of the optical/infrared galaxies from the WIRCam Deep Survey (WIRDS) catalog and used the redshifts to determine galaxies that are at the cluster redshift through a photometric-redshift cut criterion adopted from Hilton et al. (2009). The redshift cut is $1.25 < z_p < 1.67$ and a total of 30765 galaxies ($\sim$6.4 % of the total WIRDS catalog) had photometric redshifts found within this range. For galaxies with available spectroscopic redshifts, we considered a criterion where objects with a peculiar velocity that falls within ± 3 times the velocity dispersion of J2215 as associated with the cluster. A total of 1891 WIRDS galaxies with available spectroscopic redshifts found in the OII narrowband NB912+NB921 (Hayashi et al., 2017) and *GOODS*

(Stalin et al., 2010) spec-z catalogs were confirmed to be associated with J2215. In total, 31205 galaxies were associated with the cluster through both the methods with duplicates removed. For each galaxy in the WIRDS catalog we integrate the probability distribution function ($p(z)$) over the redshift interval $1.25 < z_p < 1.67$ and divide by the pixel area (in Mpc^2) to produce a projected WIRDS density map. We mask out all galaxies that do not have NIR data, that is, those that fall outside of the K_s band.

We then crossmatch the MeerKAT radio source catalog with all the galaxies found at the cluster redshift (31205 sample), and a total of 599 galaxies, which are not AGNs, were associated with a radio source. We use the Bell (2003) relation to calculate the star-formation rates (SFRs) of the 599 galaxies from their radio luminosities and we make a projected SFR per pixel area density map. Like the WIRDS density map, we mask all galaxies that do not have NIR data. Our results show that a filament structure $\approx$ 18.3 Mpc long is located along the east to the south of the cluster. The filament center is $\approx$ 4.41 Mpc ($\approx 5.5\times \mathrm{R}_{200}$ where R_{200} is approximately the cluster virial radius 0.8 Mpc) away from the cluster center. Our results qualitatively agree well with the filament structure that is seen in Hayashi et al. (2011) who used Subaru/MOIRCS data (OII emitters) to trace the filament. From the SFR density map we conclude that the filament contains some star-forming galaxies.

Preface and Declaration

Preface

The work described in this dissertation was carried out in the School of Mathematics, Statistics and Computer Science University of KwaZulu-Natal, Durban, from September 2019 to July 2022, under the supervision of Prof Matt Hilton. These studies represent original work by the author and have not otherwise been submitted in any form for any degree or diploma to any tertiary institution. Where use has been made of the work of others it is duly acknowledged in the text.

Nondumiso Khumalo

July 2022

Declaration

I, Nondumiso Khumalo, fully understand the meaning of plagiarism and hereby declare that all of the work in this document, unless stated otherwise through source acknowledgment, is my original research.

Acknowledgments

I would like to thank Prof. Matt Hilton for his constant supervision, guidance and patience throughout my project. I would also like to convey my gratitude to Prof. Subharthi Ray for agreeing to be my administrative supervisor at UKZN. I would like to thank Diana Klutse for her kindness and assistance whenever I needed help. I would like to thank my mother Thabile Ladybrite Khumalo and my church Manzolwandle Assembly for their prayers and continued support throughout my degree. Last but not least, I would not have finished this thesis if it wasn't for my Lord and Saviour Jesus Christ and for the love and grace He has shown me in this project. I am truly grateful. I was funded by the National Astrophysics and Space Science Program (NASSP) bursary and the South African National Space Agency (SANSA) for this project and I am fully grateful and thankful to them for providing me with the opportunity to do my MSc.

Contents

List of Figures

Chapter 1

Introduction

In the local Universe, the star-formation rate (hereafter, SFR) of galaxies increases with galaxy density up to the scale of galaxy groups. It then sharply declines within denser regions of galaxy clusters (e.g. Dressler et al., 1997). Since all galaxies must have been star-forming at some point, this infers that certain mechanisms in the environment must have resulted in the quenching of the star formation within the dense cluster regions. Most of these star-forming cluster galaxies lie outside the core and extend beyond the virial radius of the cluster (e.g. Santos et al., 2013). They lie on the outskirts of the clusters and are inferred to be in-falling. Also, Dressler (1980) in his paper on the morphology-density relation found early-type galaxies (elliptical and lenticular, or S0, which are not star-forming) to dominate in high-density cluster regions, and late-type galaxies (spirals and irregulars, which are actively star-forming) to dominate in less-dense cluster regions. But, Muzzin et al. (2012) found that stellar mass, rather than environment, plays a pivotal role in determining the stellar populations of galaxies, but the environment plays a different role: it controls the fraction of star-forming galaxies.

Infrared luminosities measured with the deep *Spitzer*/MIPS observations at 24 μm found that $z > 1$ clusters from the IRAC Shallow Cluster Survey (ISCS) have

substantial star formation activity observed at all radii, including the cluster cores (Brodwin et al., 2013). Also, it was observed that the fraction of star-forming galaxies increases rapidly with redshift, which implies that the environment was less hostile to star-formation in the past (e.g Dressler et al. (1997)).

X-ray selected cluster XMMXCS J2215.9-1738 from the X-ray Multi-Mirror Mission (XMM-Newton) is a well-developed, high redshift cluster that has an actively star-forming core, which Hilton et al. (2010) discovered by identifying many OIIλ3727$\mathring{A}$ emitters in the cluster core. Rich galaxy clusters are useful in measuring the effect of the environment on galaxy evolution as they cover a wide range of environmental densities; their cores are the most extreme dense regions at any epoch.

The question to ask now is do these highly star-forming galaxies extend onto the large-scale structure beyond the cluster's virial radius? There are currently no papers that have explored the SFRs in the large-scale structure beyond $z\approx1.5$, so we will aim to do this with J2215 which is at z =1.46.

We begin this chapter with a brief overview on cosmology and large-scale scale structures in Section 1.1. In Section 1.2 we will look at galaxy clusters and the various methods through which they can be detected or observed. In Section 1.3 we will discuss our selected cluster of interest, XMMXCS J2215.9- 1738. We conclude with Section 1.4 which is a motivation for our work.

1.1 Probing the Large-Scale Structure of the Universe

1.1.1 Cosmology

The large-scale structure of the Universe is assumed to be homogeneous and isotropic (e.g. Liddle, 2015). This means that it looks the same at each point in all directions at scales > 100 Mpc (e.g. Perivolaropoulos & Skara, 2022) and this is referred to as the Cosmological Principle. This principle, however, breaks down in the small-scale Universe which is highly inhomogeneous because it is made up of discrete stars, planets and galaxies, rather than smoothly distributed matter (e.g. Beisbart, 2009).

The Lambda Cold Dark Matter (ΛCDM) model, often referred to as the standard model of cosmology, is one of the successful and robust models to estimate the large-scale structure distribution and formation of the Universe. Cold dark matter is non-relativistic, non-interacting (collisionless) matter (e.g. Bond & Efstathiou, 1984). The ΛCDM model was used from the 1970s up to the 1990s (roughly), when observations showed that we don't live in an $\Omega_{m0} = 1$ universe. After the Type Ia SNe result by (Riess et al., 1998) and (Perlmutter et al., 1998), the ΛCDM model became the standard model. The ΛCDM consistutes of dark energy, cold dark matter and baryonic matter (ordinary matter).

The parameters of the ΛCDM model have been constrained to high precision within the past decade. Measurements of the angular power spectrum and lensing of the cosmic microwave background (CMB) which is relic radiation from the early Universe permeating space, from the Planck surveyor were published in (Planck Collaboration et al., 2020), with Hubble parameter $h = 0.674 \pm 0.005$.

1.1.2 Dark matter

Preceding the 1980s, it was accepted that the observable matter was not sufficient to explain the existance of the large-scale structures that we see in the Universe today. The observable matter, called baryonic matter which consists of electrons, protons and neutrons (electrons are not baryons, but are traditionally included by cosmologists), could not solely account for the vast stuctures that have formed in the Universe. This implied that there had to exist another form of matter that must have contributed to the formation of the large-scale structures. This matter is called dark matter and was first coined in a study by Zwicky (1933) in study of the peculiar velocities of the Coma cluster. He found that the peculiar velocities of galaxies in the Coma cluster were higher than those predicted by theory. This implied that there had to be other matter beyond that which is traced by the visible light emission from galaxies, and this is now referred to as 'dark matter'.

Baryonic matter is known to interact through four ways: gravity, electromagnetic force, weak force, and quantum chromodynamics (QCD), which is the strong interaction between quarks mediated by gluons. Dark matter, on the contrary, is only seen through its gravitational interaction, such as through gravitational lensing (see Figure 1.1). It is today known to make up $\approx 25\%$ of the ΛCDM universe, with dark energy and normal baryonic matter making up $\approx 70\%$ and $\approx 5\%$, respectively (Planck Collaboration et al., 2014).

1.1.3 Cosmic Web

The view of the Universe at a few to more than a hundred megaparsec-scales exhibits an inhomogeneous, web-like structure that is composed of dense regions of galaxies in long filamentry bridges, flattened sheets, and vast low-galaxy density regions called voids (see Figure 1.2). These are all intricately interconnected to

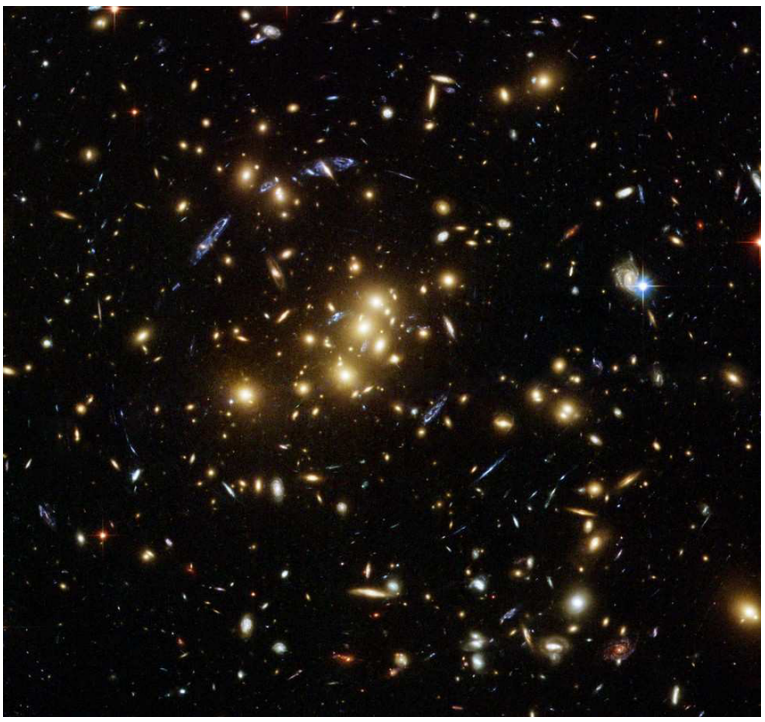

Figure 1.1: Strong gravitational lensing seen around the galaxy cluster CL0024+17. The gravitational lensing is seen as the blue streaks on the image. These are distant galaxies behind the cluster that appear as elongated arcs distorted in the image by gravitational lensing. Source: Massey (2008)

form a structure we call the Cosmic Web (Libeskind et al., 2018). Figure 1.2) illustrates the Cosmic Web structure as identified by the `NEXUS+` algorithm (Cautun et al., 2013) which identifies the density field, filaments and wall structures from real and simulated data.

The Cosmic Web formed through a process called gravitational instability which occurs when matter is gravitationally drawn closer together due to small, primordial density and velocity perturbations in the Universe (Peebles, 1982). It supposes that at an earlier time in the Universe, there were small irregularities in the distribution of matter. Regions having the advantage of higher densities would gravitationally attract more material around them and grow more in density, compared to their low density counterparts. Regions of higher densities would form clumps of matter in the form of galaxies and galaxy clusters. An irregular distribution of matter is unstable under gravity, and therefore gravitational instability would grow more irregular with time, eventually growing non-linearly. To model the non-linear regime of large-scale structure formation, N-body simulations are used.

1.1.4 Cosmological N-body Simulations

According to the ΛCDM model, cosmic structures emerged from weak density fluctuations that happened in a homogeneous and rapidly expanding early universe. These fluctuations therefore under gravity eventually resulted in the large structures that we see today. Initially these perturbations grew linearly but eventually followed non-linear growth. This means that the early structures can be calculated analytically, however the non-linear growth cannot and will need to be calculated through numerical simulations, that is, N-body simulations.

Cosmological N-body simulations are the main tool used to predict the evolution of the large-scale structure in our Universe. Different simulations exist that

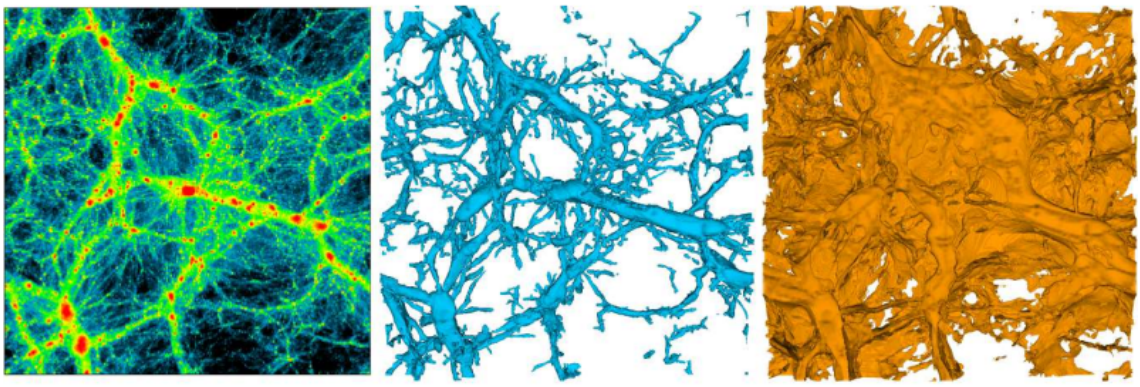

Figure 1.2: The complexity and multiscale character of the cosmic web as identified by NEXUS+. It shows the density field (left), the filaments (centre) and the walls (right) in a $100 \times 100 \times 10$ $(h^{-1}\text{Mpc})^3$ slice through the Millennium-II Simulation. Source: Cautun et al. 2016

vary in results due to the initial parameters assumed; for example, the number of particles used in the model and the initial cosmological parameters applied to tune the evolution of the model through the epochs. These are run with varying assumptions on the controlling physics. Simulations can be modeled to only include dark matter, baryonic matter and different fractions of hot and cold dark matter.

Many cosmological N-body simulations exist today due to the the growing knowledge within cosmology as well as the supercomputing power. One example of a cosmological simulation is `Illustris` (e.g. Nelson et al., 2015) which is a large volume of hydrodynamical simulations run with the moving-mesh code `AREPO` (Springel, 2010). It simulates a volume of $(106.5\text{ Mpc})^3$ starting from a redshift of $z = 127$ to the present day, z =0 and self-consistently evolves five types of resolution elements comprised of: dark matter particles, gas cells, passive gas tracers, stars and stellar wind particles and supermassive black holes.

One of the most widely used N-body simulation to date is the Millennium Simulation (MS) (Springel et al., 2005) which uses 10^{10} particles to follow the

evolution of the dark matter distribution within a cubic region of size 500 h^{-1} Mpc on a side from $z = 127$ until $z = 0$. Its successor, the Millennium II Simulation (MSII) (Boylan-Kolchin et al., 2009), is five times smaller on each side compared to the simulation box in the MS. This results in the volume sampled for MSII being 125 times smaller than the volume in MS but the mass resolution is 125 times better. Each simulation particle has a mass $6.885 \times 10^6\ h^{-1}\mathrm{M}_\odot$.

1.2 Galaxy Clusters

Galaxy clusters are one of the largest gravitationally-bound objects in the Universe. They contain about 50 to 1000 galaxies and have a diameter of ≈ 2 Mpc. Galaxy clusters are characterized by a virialized region where matter is in dynamical equilibrium, that is, a state where all galaxy populations within a cluster have distributions in velocity and position that individually reflect the same underlying mass distribution, although the derived virial masses may be different (Carlberg et al., 1997). The mean density within a virial radius r_{vir} is $\Delta\times$ the critical density ρ_c of the Universe. The critical density ρ_c of the Universe is given by

$$\rho_c = \frac{3H(z)^2}{8\pi G}, \tag{1.1}$$

where $H(z)$ is the Hubble parameter and G is the gravitational constant. Cosmological simulations usually use $\Delta \approx 200$ as this has been found to work well for scaling halo properties. The mass at $\Delta \approx 200$ is given by

$$M_{200} = \frac{4}{3}\pi r_{200}^3(200)\rho_c, \tag{1.2}$$

where r_{200} is the radius from the cluster center within which the mean density is 200 times that of ρ_c. Note that the virial radius is not the same as r_{200}, but it is a close estimate.

1.2.1 Detection of galaxy clusters

Galaxy clusters can be detected using various methods. This involves using different wavelengths in the electromagnetic spectrum to reveal their properties. We will discuss some of these below.

1.2.1.1 Optical detection of clusters

One of the first galaxy optically selected cluster catalogs was done by Abell (1958) for clusters at low redshifts ($z \lesssim 0.1$). In this paper he compiled a catalog of 2712 rich clusters of galaxies from the Palomar Observatory Sky Survey which was intended to assist with future studies of galaxy cluster properties. In the paper he also made a homogeneous sample of 1682 clusters that was useful for the statistical study of galaxy clusters. This early catalog was subject to photometric errors and projection effects. Since then, the technology used to detect clusters in the optical has improved with tens of thousands of clusters detected out to a redshift of $z \sim 1$. The redMaPPer catalog (e.g. Rykoff et al., 2016) is a more recent version of optical cluster detection that uses objective criteria, and the colours of early type galaxies in clusters (the red-sequence) to find clusters. There are, however, advantages and disadvantages of using optical methods. The catalogs obtained through this method are flux, thus redshift, limited and suffer from projection effects due to contiminants along the line of sight. The advantage is that optical methods can cover wide-sky surveys at a relatively cheaper cost than for example, X-ray surveys.

1.2.1.2 X-ray detection of clusters

One of these methods is through the mechanism of thermal bremsstrahlung. Galaxy clusters are made up of $\approx 5\%$ galaxies, 15% of intracluster medium (ICM), and 80% dark matter. The ICM fills most of the space between galaxies and if the gas shares the same dynamics as the galaxies of a cluster, then its temperature can be

approximated by

$$K_B T \simeq \mu m_p {\sigma_v}^2 \simeq 6(\frac{\sigma_v}{10^3 \mathrm{kms}^{-1}})^2 \mathrm{keV}, \tag{1.3}$$

where m_p is the proton mass and μ is the mean molecular weight ($\mu = 0.6$ for a primordial composition with a 76% fraction contributed by hydrogen) (e.g. Rosati et al., 2002), and σ_v the galaxy velocity dispersion. Because of the very high temperatures of the ICM as implied by Equation 1.3, the ICM gas behaves as fully ionized plasma whose emission is primarily through thermal bremsstrahlung. Thermal bremsstrahlung is a process whereby high-energy electrons collide with ions in the plasma resulting in them slowing down and releasing energy in the form of a photon (as energy has to be conserved). The emissivity for this process at a frequency ν scales as emissivity $\propto n_e n_i T^{-1/2}$, where n_e and n_i are the number densities of electrons and ions, respectively, and T is the temperature. Integrating this equation over an X-ray wavelength range and gas distribution, X-ray luminosities ranging between $L_X \sim 10^{43} - 10^{45}$ ergs^{-1} are obtained. These luminosities allow clusters to be identified as extended sources. J2215.9-1738 was first detected in the X-ray from the XMM Cluster Survey (XCS) (Stanford et al., 2006).

1.3 Star formation properties of galaxies in clusters

Local galaxies can be divided into two main classes: star-forming (gas rich) and quiescent (passive and gas poor). It is known that a galaxy's environment in the local universe plays a crucial role in the galaxy's properties, including its star-formation properties. Low density environments favour spirals, which are star-forming, whilst clusters (dense environments) favour ellipticals, which are non star-forming. Thus galaxies found in dense environments are often redder, older, more spheroidal and less star-forming. Typically, the central regions of clusters

are inhabited by the biggest, reddest, deadest galaxies therefore star-formation is usually lower in the cluster core.

The primary mechanism responsible for quenching star formation in galaxies is still uncertain, but there are proposed physical mechanisms that explain the environmental effect on SFRs in galaxy clusters. Stripping, or ram pressure stripping, involves the sudden removal of cold gas from galaxies through outflows from the galaxies' environment (Gunn & Gott, 1972). The removal results when the hot ICM causes drag for the galaxies moving through it, thus stripping them of their cold gas. Once the cold gas has been removed by stripping, there is no longer any fuel for star formation, and so the galaxy's stellar population evolves passively thereafter becoming "red and dead". Strangulation occurs when the supply of cold gas that is used for star-formation in the galaxies suddenly comes to a halt thus suffocating star-formation (e.g. Peng et al., 2015). This happens when a galaxy falls into a dense environment, such as a cluster, where it loses access to its cold gas reservoir. After this it makes use of the gas that it has left for star-formation until this supply is depleted and star-formation comes to an end. Galaxy harassment happens when highly star-forming disk galaxies in a rich cluster have a high-speed encounter with other galaxies. This encounter changes the morphology of the galaxies from one that is star-forming to that of little-gas, non-star-forming spheroids (Moore et al., 1996, 1998). Mergers occur when dark matter halos merge under hierarchical growth resulting in the combination of the halo baryonic-counterparts (e.g. Pearson et al., 2019). This interaction results in the disruption of the galaxies that lie at the centre of the dark matter halos. There is also a physical process that increases the star-formation rather than quench it called tidal forces. Tidal forces are a gravitational interaction that act to pull and distort the galaxies, subsequently moving stars within the galaxies from the disk to the spheroid component, causing a shock-induced star-formation.

1.4 Star-formation tracers

The light emitted from stars in galaxies can be used as tracers to the star-formation rate. A few examples of such emissions are UV, Hα, FIR and radio. The two former emissions are prone to dust-obscuration and the latter two are not. We will discuss in detail each of these tracers below (Kennicutt, 1998).

1.4.1 UV continuum emission

UV emission traces star-formation in young stars as the SFR scales with UV luminosity through the Equation 1.4 (Kennicutt, 1998). If the star-formation remains unvarying over long timescales ($\sim 10^8$ years or longer), the UV flux over a wavelength range (ideally 1250-2500$\mathring{A}$) can be used to converted to SFRs using stellar population synthesis models and an assumed initial mass function (IMF) (Kennicutt, 1998). Converting the calibration of Madau et al. (1998) using a Salpeter (1955) IMF with mass limits of 0.1 and 100 $M_\odot$ we get the following star-formation rate equation,

$$SFR\ (M_\odot yr^{-1}) = 1.4 \times 10^{-28} L_\nu(\text{ergs s}^{-1}\ \text{Hz}^{-1}), \tag{1.4}$$

where L_ν is the UV luminosity (Kennicutt, 1998). The advantage of the above method is that it provides a simplified, direct relation between the stellar population emission and the SFR. It also can be applied over a wide range of redshifts. The disadvantage is that it is highly dependent on the assumed IMF and is sensitive to dust extinction.

1.4.2 Hα

High-energy (short-wavelength) emissions from young, massive stars ionize the interstellar medium (ISM). This gives rise to re-emission in a form of recombination

lines in Hα. The re-emission in Hα can then be used to probe young, massive stellar populations(Kennicutt, 1998). The ionizing flux to SFR relation is adopted from a stellar population synthesis model which only considers stars with masses > 10 M$_\odot$ and lifetimes < 20 Myr as the main contributors of the star formation (Kennicutt, 1998). For solar abundance and applying the Salpeter (1955) IMF mentioned in Section 1.4.1 along with the calibrations of Kennicutt et al. (1994) and Madau et al. (1998) gives the relation,

$$SFR\ (M_\odot yr^{-1}) = 7.9 \times 10^{-42} L_{H\alpha}(\text{ergs s}^{-1})\ (for\ starbursts), \qquad (1.5)$$

where $L_{H\alpha}$ is the H$_\alpha$ luminosity.

The advantages of H$_\alpha$ is that it provides direct coupling between the nebular emission and SFRs. It also has high sensitivity. The disadvantages are that H$_\alpha$, like UV emission, is subject to dust extinction which may result in large systematic errors. Just like all the other methods this method depends on the assumed IMF and the assumption that all of the massive star-formation is traced by ionized gas.

1.4.3 Far-Infrared (FIR) Continuum

Most of the bolometric luminosity emitted by a galaxy is absorbed by the intestellar dust when it passes through it (Kennicutt, 1998). The luminosity is re-emitted in the thermal infrared (IR) at wavelengths ranging between 10-300 μm. The dust absorption peaks in the UV, therefore the far-infrared continuum (FIR) can be used as a tracer of young stellar populations and SFR. The efficiency of this method depends highly on the dust heating within the stellar populations and the relation between the FIR luminosity and SFR. Usingthe models of Leitherer & Heckman (1995) for continuous bursts of age 10-100 Myr as well as the Kennicutt (1998) IMF yields the equation,

$$SFR\ (M_{\odot} yr^{-1}) = 4.5 \times 10^{-44} L_{FIR} (\text{ergs s}^{-1}), \tag{1.6}$$

where L_{FIR} is the FIR luminosity integrated over the full mid and far-IR spectrum (8–1000 μm) (Kennicutt, 1998). The advantage of this method is that the FIR emission is not attenuated by dust extinction and the disadvantage is its reliance on the assumed IMF.

1.4.4 Radio emission

A tight relation is known to exist between L_{FIR} and radio emission (e.g Condon, 1992; Mas-Hesse, 1991). This implies that radio luminosity can be used as a tracer of star-formation. The radio luminosity from star-forming regions has two components: the thermal (L_{th}) and the non-thermal (L_{nth}) component. The former results from the process of bremmstrahlung, and the latter from synchrotron radiation that is emitted by electrons after being accelerated by supernovae explosions (Rubin, 1968). The spectral index differs for both; L_{th} has a spectral index $\alpha_{th} = 0.1$ (Rubin, 1968) and $\alpha_{nth} = -(0.8 - 0.9)$ for L_{nth}. (Mas-Hesse, 1991). Applying a calibration of SFR(FIR) from Kennicutt (1998), a variety of galaxy types (e.g irregular galaxies, spiral galaxies, starburst galaxies, etc) and the tight correlation between L_{FIR} and radio emission, Bell (2003) derived a non-linear expression for SFR$\langle L_{radio} \rangle$ using L_{FIR} as a proxy. It is expressed as,

$$\text{SFR}\ (\text{M}_{\odot}\,\text{yr}^{-1}) = \begin{cases} 3.18 \times 10^{-22} L, & L > L_{\text{c}} \\ \dfrac{3.18 \times 10^{-22} L}{0.1 + 0.9(L/L_{\text{c}})^{0.3}}, & L \leq L_{\text{c}} \end{cases} \tag{1.7}$$

where $L_c = 6.4 \times 10^{21}$ W/Hz is the radio luminosity of an L_*-like galaxy and $L = \langle L_{1.4\text{GHz}} \rangle$ is a K-corrected luminosity using the radio spectral index (typically assumed to be $\alpha = -0.8$). It is given by

$$\langle L_{1.4\mathrm{GHz}}\rangle[\mathrm{W/Hz}] = 9.52 \times 10^{12}\langle F_{TOTAL}\rangle[\mu\mathrm{Jy}] \times (D_L[\mathrm{Mpc}])^2 4\pi(1+\langle z_{phot}\rangle)^{1+\alpha}, \tag{1.8}$$

where D_L is the luminosity distance at the median redshift z_{phot} of all objects inside the redshift range and $\langle F_{TOTAL}\rangle$ is the integrated flux density at 1.4 GHz. Note that for Equation 1.7 we have assumed a Chabrier IMF instead of the Salpeter IMF that is assumed in Bell (2003).

In this thesis we will be using MeerKAT radio data to find SFRs within our cluster, XMMXCS J2215.9- 1738. Therefore, we will be applying this method later to calculate the SFRs. This is the first study that calculates the SFR around J2215 using radio continuum data, as other studies have done so using OII emission (Hayashi et al., 2010) or IR luminosities (e.g Hilton et al., 2009; Ma et al., 2015; Stach et al., 2017).

1.5 XMMXCS J2215.9- 1738 Galaxy Cluster

Red, quiescent (non star-forming), early-type galaxies make up the largest population in higher density environments at $z = 0$ such as in the cores of groups and clusters, whilst blue, star-forming, late-type galaxies make up the larger portion in lower density regions (Kauffmann et al., 2004). This is refered to as the star-formation rate density relation (henceforth, SFDR). However, several studies that have been conducted at higher redshifts seemed to defy this relation where the opposite seems to become true. The cluster XXMCS J2215.9-1738 (J2215) is an example of a high-redshift cluster (at $z = 1.46$) that has starburst galaxies in its core (Hayashi et al., 2010; Hilton et al., 2010). J2215 (Figure 1.3) is a good candidate to study the star-formation activities in/near the core because it is one of the most distant spectroscopically confirmed clusters discovered in the X-ray band

(Stanford et al., 2006) and its structure appears well developed. It has a velocity dispersion σ_v of 720 ± 110 kms^{-1}, implying a virial mass of $M_{cl} = 3 \times 10^{14} M_{\odot}$ (Hilton et al., 2010), from the $M - \sigma_v$ relation, which is the relation between the cluster mass (M) and the velocity dispersion of the galaxies.

Several studies have proven J2215 to have a uniquely, highly star-forming core. Hayashi et al. (2010) detected many [OII]3727 emitters in the cluster core , and Hilton et al. (2010) found several mid-IR bright, apparantly star-forming cluster members within a radius of 0.25 Mpc from the cluster center using *Spitzer*/MIPS data. These studies support the SFDR reversal within this high-redshift cluster thus making J2215 a good candidate to investigate the dependency of the star-formation or SFRs on its local environment. Further studies from SCUBA-2 (Ma et al., 2015) and ALMA (Stach et al., 2017) on J2215 confirmed that the cluster center contained star-forming galaxies. 14 galaxies were detected with 1.2 mm continuum emission, with 11 of these galaxies having CO redshifts, confirming membership to cluster. According to Ma et al. (2015), J2215 is one of the most actively star-forming clusters, with an integrated SFR of ≈ 1400 M$_{\odot}$ yr^{-1} within a radius of 0.8 Mpc. Ma et al. (2015) and Stach et al. (2017) studied the SFR in the core of the cluster within a radius of 0.8 Mpc and 0.5 Mpc from the cluster center, respectively. However, it is unknown whether this high SFR property extends farther into the surroundings of the cluster (at > 0.8 Mpc). There are currently no surveys that have undertaken to investigate the SFR activity beyond this point (> 0.8 Mpc) in the large-scale structure around J2215. We will aim to do that in this thesis.

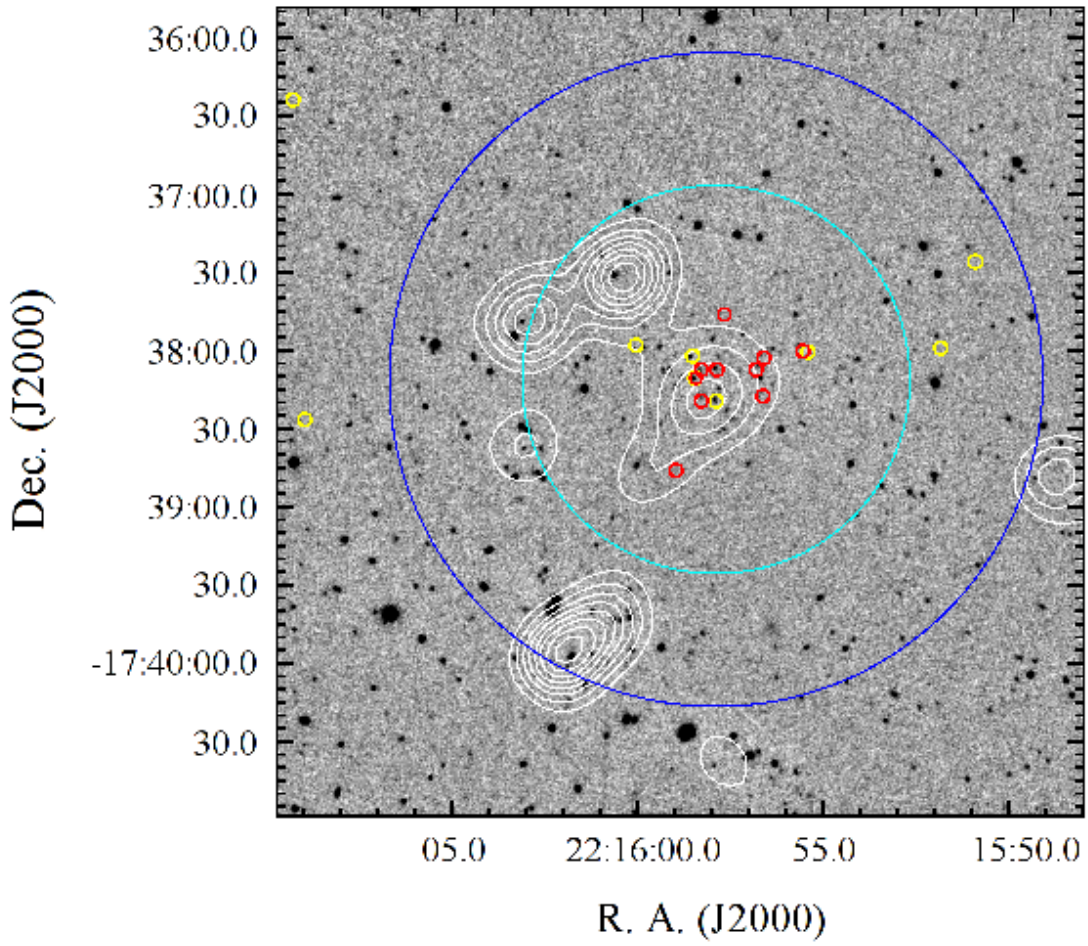

Figure 1.3: 5.2′ × 5.2′ Ks band image of X-ray selected J2215.9-1738 with X-ray contours overlaid in white. Objects spectroscopically identified as cluster members and within a projected 2 Mpc radius are highlighted. Members with z < 1.457 are highlighted in red; members with z > 1.457 are highlighted in yellow. The dark blue circle marks the cluster virial radius of 1.05 Mpc; the light blue circle marks the radius r_{200} = 0.63 Mpc, calculated from the cluster velocity dispersion. Source: Hilton et al. (2007)

1.6 Motivation

In this thesis, we use MeerKAT observations to identify potentially star forming galaxies in the large scale structure around J2215. With the help of MeerKAT's degree field of view (FOV), we will aim to identify galaxies with SFRs $> 40 M_{\odot}\,\mathrm{yr}^{-1}$ (comparable to SFRs reported in (Stach et al., 2017)) across the cluster and up to a radius of ≈ 15 Mpc into the surrounding large-scale structure and beyond. We will be aiming to spot interesting star formation from infalling galaxies beyond the virial radius. To accomplish this we will need multiwavelength data that will help us identify MeerKAT sources at the cluster redshift. Fortunately, J2215 is found in one of the CFHT Legacy Survey (CFHTLS) deep fields, the D4 field (see Bielby et al., 2010). The CFHTLS D4 field provides deep optical data ($griz$) combined with the near-infrared (JHK) imaging from the WIRCam Deep Survey (WIRDS). The CFHTLS D4 field is beneficial to us as it overlaps with most of the MeerKAT field, meaning that we can use it to measure photometric redshifts of radio sources in the large scale structure around J2215. This is the first study of calculating SFRs around J2215 using radio continuum data since previous studies have done so using OII emission (Hayashi et al., 2010), or IR luminosities (e.g Ma et al., 2015; Stach et al., 2017).

In Chapter 2 we will discuss the data we used, that is the MeerKAT radio data and the optical/infrared (IR) data from CFHTLS. In Chapter 3 we discuss the methods and the samples we used to make density maps, as well as to calculate SFRs. We discuss each of the density maps in detail. In Chapter 4 we discuss the star-forming groups and filamentry structures traced around J2215, and in Chapter 5 we close with conclusions. Throughout this thesis, we use the cosmological parameters $\Omega_{\Lambda} = 0.7$, $\Omega_m = 0.3$ and $H_0 = 70\,\mathrm{kms}^{-1}\,\mathrm{Mpc}^{-1}$.

Chapter 2

Data

To identify the large-scale structure around the J2215-1738 cluster, we use the MeerKAT radio telescope which provides us with radio imaging data to spot filaments at the cluster redshift $z = 1.46$. We needed multiwavelength data to assist us in identifying MeerKAT radio sources at the cluster redshift. Fortunately, the WIRCam Deep Survey (WIRDS) has deep optical ($ugriz$) and near-IR (JHK_s) imaging data available (e.g. Bielby et al., 2010), sufficient to compile robust photometric redshifts for galaxies at $z \sim 1.5$. We also include in this chapter a section on the spectroscopic catalogs that we will use later to calibrate the photometric redshifts that we calculate.

2.1 CFHTLS Optical and WIRDS Near-IR Data

The optical data in the five optical bands ($ugriz$) that we use in this thesis is taken from CFHT as part of the CFHT Legacy Survey (CFHTLS) (Bielby et al., 2012). The CFHTLS consists of four independent 1 deg^2 deep fields, namely the D1, D2, D3 and D4 fields and J2215 is found in the D4 field, which has its center positioned

at 22:15:31 -17:43:56 [1].

For near-infrared (near-IR) data we use the *J, H* and K_s band data observed with WIRCam detector on CFHT in the WIRCam Deep Survey (WIRDS) which covers $\sim 0.4\text{deg}^2$ of the CFHTLS D4 field (Bielby et al., 2010). WIRDS comprises extremely deep, high quality (FWHM (full width at half maximum) $\sim 0.6''$) *J, H* and K_s imaging covering a total effective area of 2.1 deg^2 and reaching AB [2] 50% completeness limits of ≈24.5 in all the three bands (*J, H* and K_s) (Bielby et al., 2012). A catalog is publicly available that provides a combination of the near-IR and optical data (*ugrizJHK*$_s$) of the D4 field. The *J, H* and K_s band data is important because it provides NIR data that helps us find reliable photometric redshifts at the cluster redshift of z =1.46.

The catalog that we used combines both the *ugriz* and *JHK*$_s$ into one catalog with a *ugrizJHK*$_s$ dataset and can be downloaded from the Canadian Astronomy Data Center (CADC)[3], where it is listed as *WIRDS_D4-95_grichi2_ugrizJHKs_221531-174356_T0002.cat* (Bielby et al. (2012)). This is a Terapix-produced catalog [4] and the data was collected with the wide-field optical and near infrared imager MegaCam on the Canada-France-Hawaii Telescope (CFHT). Terapix is a data-processing pipeline (primarily used to process MEGACAM data). This combined catalog (which we will refer to as the WIRDS catalog throughout the thesis) has a total of 483940 galaxies in the D4 field.

[1] https://www.cfht.hawaii.edu/Science/CFHLS/cfhtlsdeepwidefields.html

[2] The AB system is an astronomcal magnitude system that sets the zero-point for monochromatic magnitudes, specifically setting it such that zero represents 3631 Jy.

[3] https://www.cadc-ccda.hia-iha.nrc-cnrc.gc.ca/en/cfht/wirds.html

[4] https://cadcwww.dao.nrc.ca/cfht/cfhtls/T0007.html

2.2 MeerKAT data

MeerKAT is located in the Northern Karoo region of South Africa and has 64 interlinked antennas, with the longest baseline between any two antennas being 8 km. Three receivers on MeerKAT are expected to cover three different bands on the radio spectrum: the UHF (580- 1015 MHz), L (900- 1670 MHz) and S (1750-3500 MHz) band (e.g. Asad et al., 2021), however the latter is not available as yet. We use the *L*-band data to identify radio sources at our cluster redshift.

The total integration time for the entire observation was $\approx$ 16 hours and the RMS that was measured in the final image was 3.5μ Jy beam $^{-1}$. The MeerKAT data was obtained as part of an open time program (PI: M. Hilton; Proposal ID: SCI-20190418-MH-01) on 11-12 May 2019. The observations were split into two blocks, each of duration 6.2 hours. The data was obtained with the 4096 channel correlator, which resulted in 209 kHz channel resolution. The data was recorded in full polarization with a correlator dump of 8 seconds, and the data was acquired for all polarization products, namely XX, XY, YX and YY. The primary calibrator for flux, delay and bypass calibration was J1239-6342, while the closer source (i.e., $\approx$ 13 degrees of the target source position), J225-0457 (3C446) was used as the secondary calibrator (for amplitude and phase calibration). The WIRDS D4 field overlaps with the MeerKAT field (see Figure 2.1). We will use the flux obtained from the MeerKAT catalog to calculate radio luminosities (see Equation 1.8) that we will then convert to SFRs (see Section 1.4.4).

2.2.1 MeerKAT data processing

In this thesis we use an image produced by Klutse et al. in prep. using MeerKAT data. The image contains MeerKAT radio-source galaxies that were selected using

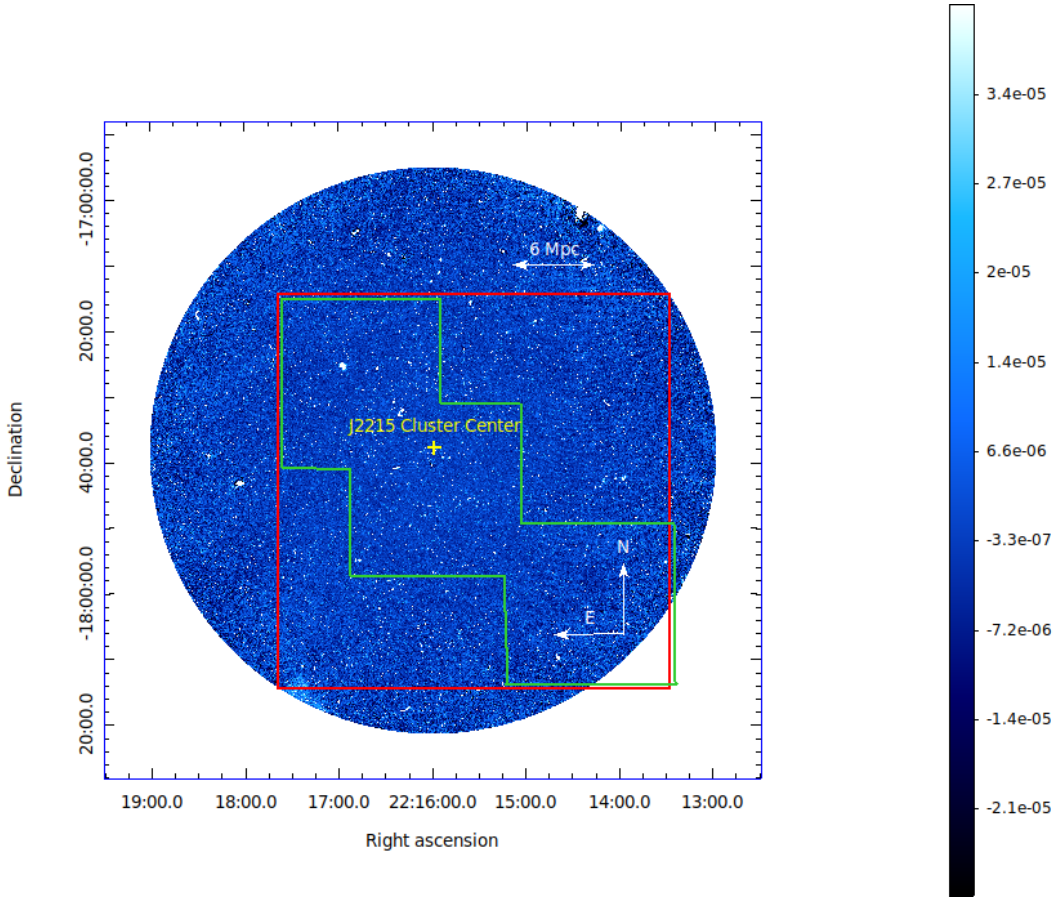

Figure 2.1: Primary beam corrected ∼1 deg^2 MeerKAT radio image of J2215.9-1738 to a RMS depth of 3.5μ Jy beam $^{-1}$ (Heywood, 2020) showing the CFHTLS D4 field outlined in red, and the WIRDS field outlined in green. The cluster center is at RA and Dec coordinates 22:15:58.5, -17:38:2.5. The color units for this image are in Jy beam^{-1}.

the Python Blob Detector and Source Finder (PyBDSF) software [5]. The PyBDSF also calculates and provides the radio flux for each of the sources found. A 4σ detection threshold was used which led to the detection of $>$ 10000 radio sources with a false positive detection rate of $\approx$ 1.4%. Within this image there was a 4.6

[5]https://pybdsf.readthedocs.io/en/latest/

Jy bright source near the cluster that was removed through peeling. The resulting 1.28 GHz image has RMS noise level of $\approx 3.5\mu$Jybeam^{-1} and a synthesized beam size of $6.01'' \times 5.26''$ with a position angle (PA) of -1°. The on-source time on target was 12 hours.

2.3 Spectroscopic redshift catalogs

We have in possession two catalogs within which some of the galaxies in our WIRDS catalog are found. The first is a *GOODS* spectroscopic catalog from Stalin et al. 2010 obtained via private communication with Richard Bielby. This catalog contains columns of the RA Dec position, object type and spectroscopic redshifts (thereafter spec-zs). The spectroscopic data from this catalog was obtained with the AAOmega spectrograph which is on the Anglo Australian Telescope. Further details on this catalog are found in the Stalin et al. 2010 paper. The second spec-z catalog contains OII-narrowband selected galaxies in the D4 field. It contains columns of ID number, RA Dec position, emission-line OII fluxes, and spec-z from Hayashi et al. 2017. More details on this catalog can be found in this paper. Spectroscopic redshifts have really small uncertainties which can be considered to be negligible in the context of the work presented in this thesis.

Chapter 3

Analysis and results

Recall that we aim to trace star formation in groups and filaments around J2215-1738. To do this, we will need to make projected density maps that will show us the surrounding structures of the cluster. We find the photometric redshifts of the WIRDS D4 field galaxies using photometric redshift code EAZY (Brammer et al., 2008), and identify galaxies that are at the cluster redshift through photometry. We also identify these galaxies by using the NB921+NB912 OII emitters with available spectroscopic redshifts. We combine all the galaxies identified through photometry and spectroscopy and crossmatch them with the MeerKAT source catalog. We then use the luminosity of the MeerKAT sources associated with the galaxies to calculate SFRs. We make projected galaxy density maps of the: i) the probability distribution function $p(z)$ of all the galaxies from the WIRDS catalog, ii) the SFRs calculated from galaxies associated with the cluster, and iii) the number density of the galaxies in the D4 field. We then use contour overlays to compare the density maps.

3.1 Photometric redshift estimation

Spectroscopic redshifts are not available over most of the D4 field, so we use the multiband ($ugrizJHK_s$) data from WIRDS to calculate photometric redshiftss (also referred to as photo-zs). The spectral energy distribution (SED) of a galaxy consists of a set of measurements of the flux of a galaxy at different wavelengths. The SED of a galaxy is then compared to the redshifted templates of the same galaxy type in the rest frame, by using the transmission curve of the filters, to determine the best fit and thus the corresponding redshift (Gomes et al., 2018). Some SED fitting methods use a library of observed or synthetic SED templates of galaxies with various stellar population properties such as age and star-formation history. The observed fluxes are then fitted to a linear combination of the templates, often through a χ^2 minimization to find the set of templates that give the closest match which leads to finding the corresponding redshift.

The SED template fitting method works because SEDs have a distinguished shape of the continnum and also have strong spectral properties such as the $4000\mathring{A}$ break and strong emission lines from active galactic nuclei (AGNs) and star-forming galaxies, respectively (Bolzonella et al., 2000). However, there are some advantages and disadvantages associated with this method. The advantage is that they allow easy extrapolation which makes it good to be used on very faint galaxies which have limited spectroscopy. Also, it allows the determination of other physical properties of galaxies such as stellar-mass and SFRs. The disadvatage, however, is that there may be a template mismatch due to template set incompleteness (Csabai et al., 2003) or when there are too many galaxy templates that it results in colour-redshift degeneracies (Benítez, 2000). However, some SED template fitting is sometimes combined with Bayesian techniques such that galaxies with known spec-z's and similar properties to the observed galaxies are used as priors to calibrate the templates (e.g Ilbert et al., 2006). This way often improves

the results as well as provide a probability density function that also provides the uncertainty in the photo-z estimates.

3.1.1 EAZY: Photometric redshift code

We used the SED template-fitting code EAZY (Easy and Accurate Z-phot from YALE; (Brammer et al., 2008)) on our 483940 WIRDS catalog to estimate our photometric redshift. EAZY uses an algorithm that steps through a user-defined range of redshifts, and at each redshift finds the best-fitting synthetic template spectrum by minimizing

$$\chi_{z,i}{}^2 = \sum_{N_{filt}}^{j=1} \frac{(T_{z,i,j} - F_j)^2}{(\delta F_j)^2}, \tag{3.1}$$

where N_{filt} is the number of filters, $T_{z,i,j}$ is the synthetic flux of the template i in filter j for redshift z, F_j is the observed flux in filter j, and δF_j is the uncertainty in F_j (Brammer et al., 2008). Unlike other SED template-fitting that look to find the best-fitting template T_i, EAZY rather finds the best fitting linear combination of a set of templates, by finding the best fit coefficients, α_i, in

$$T_z = \sum_{N_{temp}}^{i=1} \alpha_i T_{z,i}, \tag{3.2}$$

with all $\alpha_i \geq 0$. The number of templates that can be fit simultaneously in a run is one, two, or all of the templates available in the user-defined list. For the one- and two- template-fit option the coefficients α_i are determined using analytic least-square fits whilst for the "all" option the coefficients for every template in the library is determined iteratively following the algorithm of Sha et al. 2007.

3.1.2 Estimating photo-zs using EAZY

To estimate photo-zs EAZY (Brammer et al., 2008) needs a few input parameters from the user. These parameters can be input or altered within the EAZY ascii file *zphot.param.default*. Within *zphot.param.default* there are parameters that can be altered such as filters files (text file containing filter response curves), templates, wavelength file, input catalogs, priors, etcetera. However, should these not be changed by the user, EAZY offers default inputs within the *zphot.param.default* that can be used. Below are the parameters that we changed in the *zphot.param.default* settings and the rest remained the same (at EAZY initial default settings).

3.1.2.1 Input catalog

First, we need to provide EAZY (Brammer et al., 2008) with an input catalog. We use the *WIRDS_D4-95_grichi2_ugrizJHKs_221531-174356_T0002.cat* optical and NIR catalog (see Section 2.1) which contains the AB magnitude in the *ugrizJHK$_s$*-band. However, EAZY requires the catalog to have flux input rather than the AB magnitudes provided by the catalog. Therefore, we convert the magnitudes in the catalog to fluxes using the equation,

$$F_{AB} = 3631 \times 10^{\frac{-m_{AB}}{2.5}}, \tag{3.3}$$

where m_{AB} is the magnitude in the AB system where the flux zero-point in every filter is defined as 3631 Jy. We likewise converted the magnitude errors to flux errors using the

$$F_{err} = \frac{F_{AB} \times m_{err}}{2.5}, \tag{3.4}$$

where m_{err} is the error in the magnitude through each passband. We then create a new catalog specially made for input in EAZY which contains the flux

F_{AB} and F_{err} through each bandpass. EAZY contains a special file called *FILTER.RES.latest.info* that contains some of the filters from various surveys. Each filter corresponds to a unique row number that EAZY can associate with that particular filter. The row numbers in this file that correspond to the CFHTLS *ugriz* filters are F88, F89, F90, F91 and F92, respectively, where F refers to the flux through that particular filter. These filter numbers correspond to errors through each filter represented by E88, E89, E90, E91 and E92, respectively, where E refers to the flux error through that particular filter. The WIRDS J, H and K_s filters were not found on EAZY, therefore we opted to use the ESO-NTT/SOFI (European Southern Observatory- New Technology Telescope/SOFI) JHK_s filters instead. These bands correspond to row numbers F30, F31 and F32 in the filter file respectively, and flux errors E30, E31 and E32. The new catalog which we will refer to as "WIRDSALL.cat" contains columns of ra, dec, F88, F89, F90, F91, F92, F88, F89, F90, F91, F92, E88, E89, E90, E91, E92, E30, E31 and E32 for the $ugrizJHK_s$ passbands. The catalog also contains a column `z_spec` which allows spectroscopic redshift to be included if available. We put the WIRDSALL.cat as an input catalog onto EAZY.

3.1.2.2 Input template-set and wavelength file

In *zphot.param.default* we change the input for *TEMPLATE_FILE* by applying SEDs from the i) *br07_default.spectra.param* from Blanton & Roweis 2007, *eazy v1.0* from Brammer et al. 2008 and *cww+kin* (Coleman, WU, and Weedman + Kinney) from (Coleman et al., 1980; Kinney et al., 1996) template sets, all run with the "a"mode for *TEMPLATE_COMBOS* . This means that all the SEDs within the template-sets are combined simultaneously when EAZY (Brammer et al., 2008) is run.

We also use the *EAZY_v1.1_lines/lambda_v1.1.def* wavelength limit definition

file when running EAZY for each of the template sets. We selected to use this wavelength file because it seems to be the only wavelength file available on EAZY.

3.1.2.3 Bayesian priors

Oftentimes the template-fitting method suffers from color-redshift degeneracy. This means that for particular SED-colors the method fails to distinguish at which unique redshift a galaxy exists. For example, relatively featureless blue SEDs can be fit equally well at $z = 0$ and $z \sim 3$ because the templates are unable to distinguish blue colours redward of the Balmer and Lyman breaks, respectively. To eliminate this, Benítez 2000 was the first to develop a Bayesian approach to estimating photometric redshifts through the set of Bayesian priors. Priors provide additional information besides the observed photometric colors to help constrain the redshift estimates. We used *prior_K_extend.dat* as our prior input.

3.1.2.4 Output

After EAZY (Brammer et al., 2008) is run with the above *zphot.param.default* settings for each of the template sets, an output of a probability density function ($p(z)$) is produced as well as a new catalog containing ID numbers, spec-$_z$ if it was available from the input catalog, the redshift estimations, amongst others. The output catalog contains varoius photo-z estimations, however, we select to use the `z_a` which is the redshift where χ^2 is minimized for all-template linearcombination modes, before applying the prior.

3.1.3 Accuracy of the photometric redshifts

We check the accuracy of the photo-z estimates produced by EAZY (Brammer et al., 2008) by comparing them with spectroscopic subsamples described in Section 2.3 which are a total of 1973 galaxies with available spec-z. We crossmatched

both the spec-z catalogs with the WIRDS catalog using `Topcat` [1]- an interactive graphical viewer and editor for tabular data. We crossmatched between the positions of the catalogs by applying a $5.5''$ crossmatching separation radius between the WIRDS and spectroscopic catalogs (we adopted the $5.5''$ crossmatching radius between radio and optical/NIR catatogs from Section 3.4.2. After this we determined the $1\,\sigma$ scatter in the z_p vs z_s graph (Figure 3.1, 3.2 and 3.3) between the photo-z and spec-z. Note that not all the photo-zs will be plotted, but only the ones with a corresponding spec-z. The typical scatter σ_{δ_z} in photometric redshift residuals $\delta_z = \dfrac{z_s - z_p}{1 + z_s}$ was found to be 0.052, 0.043 and 0.052 using the `eazy_v1.0`, `br07` and `cww+kin` templates, respectively, with all the rest of the parameters such as priors kept the same (see Figures 3.1, 3.2 and 3.3). This means that `br07` template set produced the best photo-z results with the least scatter of $\sigma_{\delta_z} = 0.043$. Within our plots we use `odds`, a parameter in the output catalog that represents the fraction of the total integrated probability that lies within $\pm\Delta z$ of the photo-z estimate, and is designed to identify sources that have broad and/or multi-modal probability distributions (Benítez, 2000). We created a mask that selects photo-zs that have `odds` > 0.9. We plot all the calculated photo-zs in blue dots that have any `odds` value and the photo-zs that have `odds` > 0.9 in orange. Some of the photo-zs are way off the spec-zs (see Figures 3.1, 3.2 and 3.3) and this happens sometimes and was expected. This may be because the photo-zs are estimated by template fitting, and sometimes the max likelihood may have multiple solutions for the photo-z that are far from the true spec-z. Or sometimes the galaxy has a SED that isn't covered by the chosen template set, and thus its photo-z estimation deviates significally from the true z.

[1] http://www.star.bris.ac.uk/ mbt/topcat/sun253/sun253.html

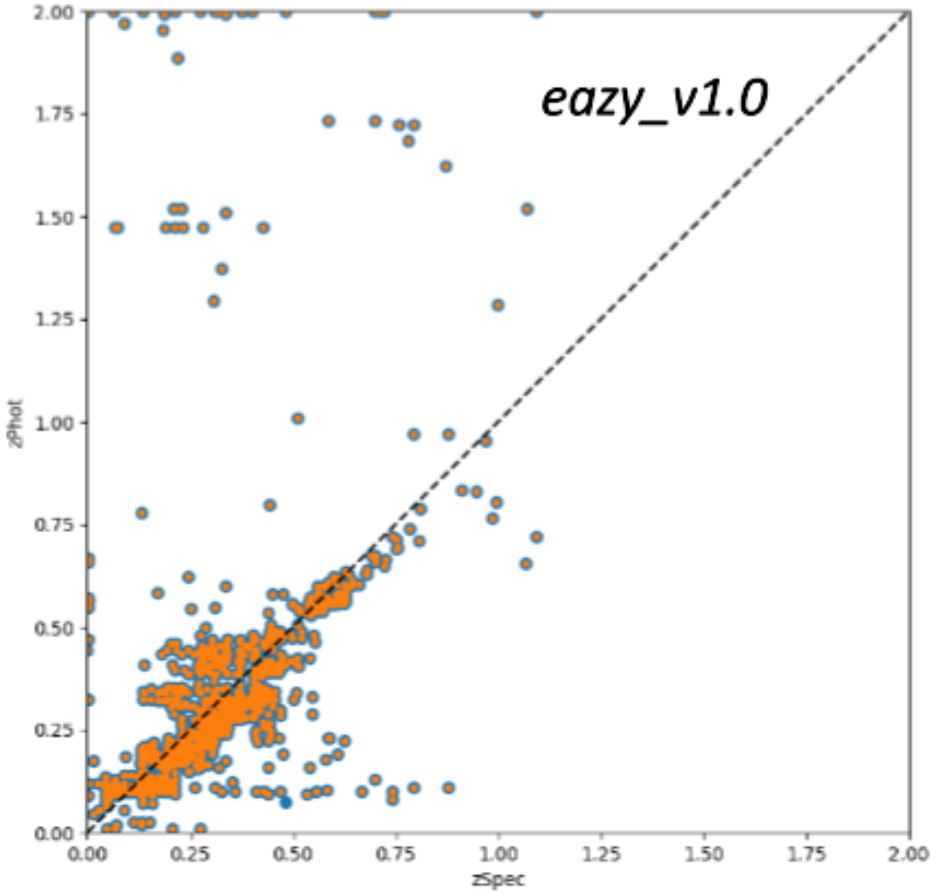

Figure 3.1: Photometric vs spectroscopic redshifts using the EAZY `eazy_v1.0` SED template set from Brammer et al. 2008 where the typical scatter in the photometric redshift residuals δ_z is $\sigma_{\delta_z} = 0.052$. The photo-$z$s that have `odds` > 0.9 are represented by the orange circles and the those with any `odds` in blue circles. The dotted line represents a 1:1 relation for comparison between photometric and spectroscopic redshift.

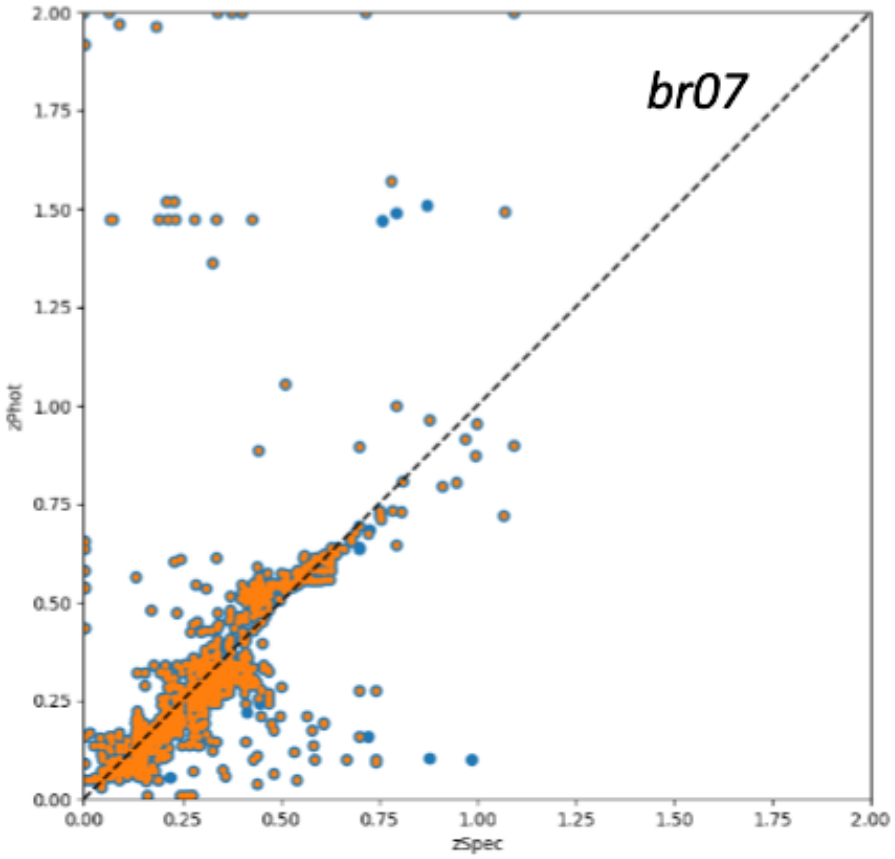

Figure 3.2: Photometric vs spectroscopic redshifts using the EAZY br07 template set from Blanton & Roweis 2007 where the typical scatter in the photometric redshift residuals δ_z is $\sigma_{\delta_z} = 0.043$. The photo-$z$s that have `odds` > 0.9 are represented by the orange circles and the those with any `odds` in blue circles. The dotted line represents a 1:1 relation for comparison between photometric and spectroscopic redshift.

3.2 Projected Density Maps

To make the density maps we start by creating a blank, square pixel map with a World Coordinate System (WCS). We center the blank map at the (RA, Dec)

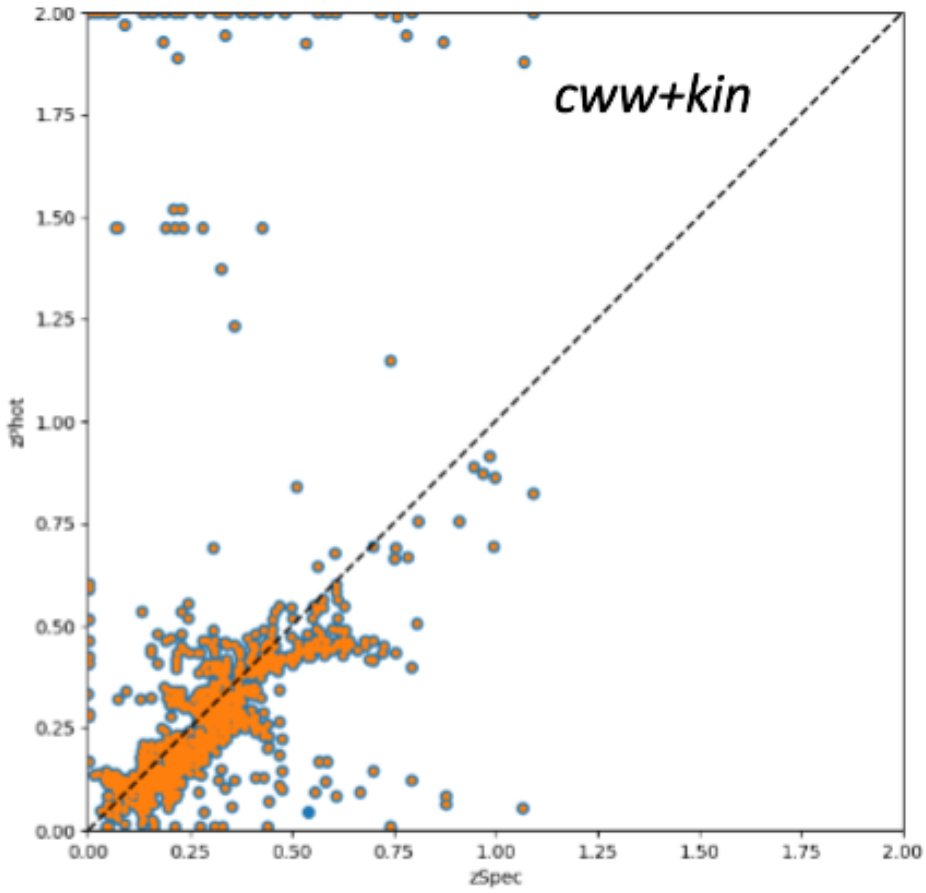

Figure 3.3: Photometric vs spectroscopic redshifts using the EAZY `cww+kin` SED template set from Coleman et al. 1980, (Kinney et al., 1996) where the typical scatter in the photometric redshift residuals δ_z is $\sigma_{\delta_z} = 0.052$. The photo-$z$s that have `odds` > 0.9 are represented by the orange circles and the those with any `odds` in blue circles. The dotted line represents a 1:1 relation for comparison between photometric and spectroscopic redshift.

coordinates (22h15m30.783s -17d44m02.378s). We chose the pixel size of the map to be a 50 pixel by 50 pixel size of the 1 deg × 1 deg D4 CFHTLS image as we agreed that fewer, chunky pixels presented the details of the image better. We tried using smaller pixel sizes (e.g 100 pixel by 100 pixel for the 1 deg × 1 deg image), however these resulted in an image that was too sparsely sampled, in terms of the number of galaxies per pixel. Therefore, the number of pixels used was determined through trial and error until we subjectively decided on which one looked best to use.

We then find the projected distance of the J2215-1738 cluster at $z = 1.46$. We used an online cosmology calculator [2] to find the projected distance of the cluster using only its redshift. The angular diameter distance calculated for $z = 1.46$ is 1743 Mpc when applying the cosmological parameters given in the introduction in Chapter 1. This gives a scale of 8.452 $\times 10^{-3}$ Mpc/″. Each pixel area is thus 0.61 Mpc × 0.61 Mpc, $\sim 72'' \times 72''$. For each of our density maps, we will mask out galaxies that do not have NIR data.

3.2.1 WIRDS D4 Field Density Map

To make our first density map we integrate the probability distribution function $p(z)$ for each of the 483940 galaxies in the WIRDS catalog, within some redshift range. We chose the integration limits to be $1.25 < z_p < 1.67$ from considering the following relation adopted from the Hilton et al. 2009 paper,

$$|z_p - z_{cl}| < 2 \times \sigma_{\delta_z}(1 + z_{cl}), \tag{3.5}$$

where z_{cl} is the redshift of the cluster, and $\sigma_{\delta z} = 0.043$ (see Section 3.1.3 above). A total of 30765 galaxies, 6.36 % of the total WIRDS galaxies, are confirmed as

[2] https://www.astro.ucla.edu/ wright/CosmoCalc.html

objects at the cluster redshift through this criterion. Note that some of these galaxies are found outside of the K_s band region (i.e do not have NIR data).

We add the value of the integral of $p(z)$ between $1.25 < z_p < 1.67$ for each galaxy to the corresponding pixel in the map where the galaxy is found, and divide by the projected area (in Mpc^2) of the pixel. This builds up a projected galaxy density map, of the region surrounding the cluster, at the cluster redshift. We then apply a mask to the 30765 galaxy-sample density map that removes all galaxies that do not have NIR data. We call this masked map the WIRDS density map and it is shown in Figure 3.4. Note that while CFHTLS optical data covers the entire D4 field, we have masked the density map to only include the region of the D4 field that has K_s-band coverage from WIRDS, as near-IR data are essential for measuring photo-zs of galaxies at the redshift of J2215. Therefore, we will be focusing on this region in our analysis.

In Figure 3.5 we encircle four significant areas with black circles and we name these regions A, B, C and D. These regions represent sites on the image that have a high density, that is, they have a relatively higher number of WIRDS optical/infrared galaxies per Mpc^2 area compared to the rest of the image. The size of each circle was chosen arbitrarily to cover the entire area of the dense region. The aim was to try and subjectively capture the area bounding each region. The diameters of A, B, C and D are 3.56 Mpc, 3.71 Mpc, 3.31 Mpc and 3.70 Mpc, respectively. We notice that the J2215-1738 cluster core region, defined in Hilton et al. (2010) as a circle with a radius of $1.55'$ (0.8 Mpc), is embedded within region D (see Figure 3.5).

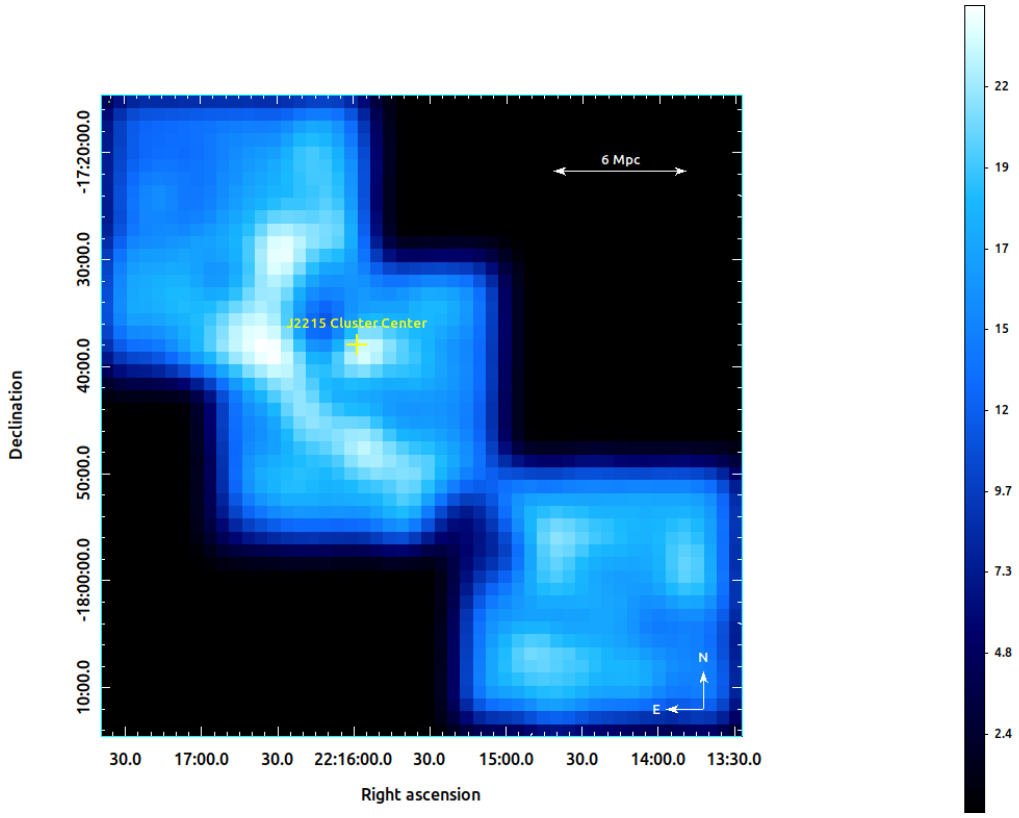

Figure 3.4: WIRDS density map in the D4 field with the galaxies that do not have *Ks*-band data masked. The J2215-1738 cluster center is marked by a yellow +. The color units for this image are in galaxies per square Mpc.

3.3 Filament-like structure

A large-scale C-shaped structure seems to be traced out by regions A, B and C (see Figure 3.8). This C-shaped structure resembles a filament shape and seems to be existing near the cluster. Note that we call this a "filament-like"stucture because we cannot confirm it as one yet due to the limitations of our largely photometric redshift sample. However, Hayashi et al. (2011) observed a similar structure at this position which they refer to in the paper as a filament (see Section 4.2). To isolate the filament-structure from the rest of the image we used the "scale parameters"

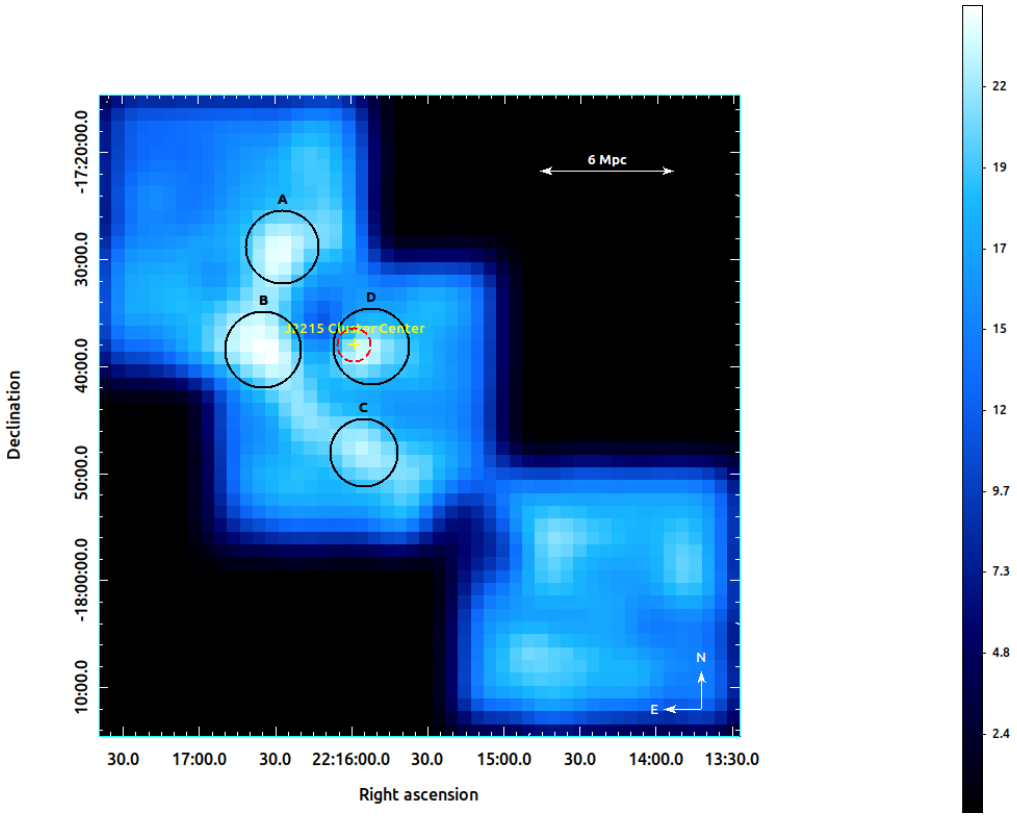

Figure 3.5: WIRDS *Ks*-band galaxy density map of the D4 field. The regions of significant (higher) density are marked by circles labeled A-D. The cluster center is marked by a yellow "+". The virial radius of the cluster, 0.8 Mpc, is shown within the dotted red circle. The color units for this image are in galaxies per square Mpc.

feature on `DS9` by selecting a threshold of 19.5 Mpc^{-2}, meaning that the WIRDS map will only be constrained to values lower than or equal to 19.5 Mpc^{-2}. The reason why we chose this threshold is because we found that 19.5 Mpc^{-2} outlines the shape and/or size of the filament-like structure quite well. The threshold range that we determined to reasonably give the shape of the filament-like structure was 18-20 Mpc^{-2}. However, looking at Figure 3.6, we can see that the threshold 19.5 Mpc^{-2} seems to represent the filament-like structure better than the rest, even

though this is subjective because we do not know the acual size of the structure.

Using the measuring vector tool found on DS9 that draws a vector (direction and magnitude), we measure the distance from the cluster center to the centers of region A, B and C. We determine these distances to be 11.89′ (∼6.13 Mpc), 8.55′ (∼4.41 Mpc), and 10.13′ (∼5.22 Mpc), respectively (see Figure 3.7). Furthermore, to determine the length of the filament-like structure we draw a vector from the top tip of the filament-like structure to the midpoint of the C-shape (taken as center of region B). We then draw another from the midpoint of the C-shape to the bottom tip of the C-shaped filament-like structure. The lengths were 14.77 ′ and 20.07 ′, repectively. This adds to a total length of $14.77' + 20.27' = 35.04'$ (∼18.07 Mpc) (see Figure 3.8). Note that the selection of the endpoints of the filament-structure is subjective as I decided which will be the starting and ending points of the structure.

3.4 SFR/Area Density Map

3.4.1 Galaxies at the cluster redshift

The first criteria extracted from (Hilton et al., 2009) selects WIRDS optical/infrared galaxies that have a z_p that fall within a redshift range determined by Equation 3.5. Recall that in Section 3.1.3 we derived $\sigma_{\delta_z} = 0.043$ for the WIRDS galaxies with available spec-z (refer to Figure 3.2). This gives a redshift interval of $1.25 < z_p < 1.67$. A total of 30765 galaxies, 6.36 % of the total WIRDS galaxies, were confirmed as galaxies at the cluster redshift through the first criterion (Section 3.2.1). Additionally, a second criterion is used that uses the WIRDS galaxies that have available spec-zs to find galaxies associated with the cluster. We use two available spectroscopic-redshift catalogs (See Section 2.3) to look for the spec-zs of some of the WIRDS galaxies. This is done by crossmatching between the

spec-z-catalogs and the 483940 WIRDS-galaxy catalog using a crossmatch radius of $1''$. This is the typical crossmatch radius that is used to crossmatch between optical catalogs. We use the spec-zs to calculate the peculiar velocity of a galaxy at redshift z in the rest-frame (spectroscopic redshift) of a cluster at redshift z_{cl} with equation

$$v_{pec}^{rest} = c(z - z_{cl})/(1 + z_{cl}). \tag{3.6}$$

If the galaxy has a peculiar velocity that falls within ± 3 times the velocity dispersion of the cluster, it is considered as associated with the cluster. The J2215-1738 cluster velocity dispersion σ_v is 720 ± 110 km s^{-1} according to Hilton et al. 2010. A total of 1891 WIRDS galaxies with available spec-z are confirmed as galaxies at the cluster redshift through this criterion.

Now that we have found the number of galaxies at the cluster redshift from both criteria, we need to eliminate any mutual galaxies from both matches, leaving only unique matches. This is because some galaxies at the cluster redshift may be confirmed using either criteria, thus appearing or being counted twice. To eliminate this we compare between both matches, removing any common entries only leaving one to count. We use the unique ID number of each galaxy to avoid re-count. Of the 30765 (criteria 1) + 1891 (criteria 2)=32656 galaxies associated with the cluster through both methods, a total of 31205 unique matches were made. This means that 1451 galaxies were occuring in both these samples, making it $\sim 76.7\%$ of the spectroscopic redshift-matched sample that are duplicated in the photometric sample in the cluster redshift range.

3.4.2 Cross matching

We crossmatch the Section 3.4.1 sample of 31205 galaxies (the confirmed number of WIRDS galaxies at the cluster redshift) associated with the MeerKAT radio

source catalog to determine which of the galaxies at the cluster redshift have a radio source. To crossmatch the MeerKAT catalog with the galaxies we need to first find a decent crossmatch radius that will ensure that we find the correct counterpart when matching the radio and optical/infrared galaxies, since these were observed at different wavelengths. Finding a good crossmatch radius also ensures that we do not overlook any matches between the two catalogs. The procedure would be to select one of the catalogs as a reference (we use the MeerKAT catalog as our reference) and use the position of each galaxy to compare to the galaxy positions from the second catalog. Galaxies that fall within the crossmatch radius are considered the same galaxy from both the catalogs.

To find the best crossmatch radius we arranged a set of 121 potential crossmatching radii ranging between 0 and 60 arcseconds. For each radius we crossmatch the two catalogs and count the number of matches obtained from each. We use randomized positions offset by $1''$. F is the fraction of the number of matches found for each radius over the maximum number of matches found across all the radii. F_{random} is the number of matches found for offset galaxy positions over the maximum number of matches observed for the randomized positions. We plot the difference $F - F_{random}$ against the crossmatch radii as shown in Figure 3.9. This figure shows that the best radius to crossmatch between the catalogs is approximately $6''$. We therefore decide to use $5.5''$, which is reasonably close to $6''$, to crossmatch between the optical/infrared WIRDS catalog with the MeerKAT radio source catalog. We choose $5.5''$ to avoid missing any genuine matches. Where the $F - F_{random}$ curve goes flat, increasing the matching radius is not increasing the fraction of matched objects, so increasing it beyond that is only going add things which are not really matches (i.e. spurious associations). After crossmatching the MeerKAT catalog with the 31205 galaxies at the cluster redshift, a total of 1051 objects were confirmed as radio sources.

3.4.3 Star Formation Rates and AGN

After finding galaxies at the cluster redshift that have a MeerKAT radio source, we may now use the radio luminosity (in Jy) to find the SFRs of these galaxies using the Bell method (Bell, 2003) explained in Section 1.4.4.

However, before calculating SFRs from the radio sources we first need to take careful consideration of one critical hindrance: active galactic nuclei (AGN). We need to account for these AGNs which may misleadingly pass as highly star-forming galaxies. To avoid contamination by AGN in our sample, we remove all galaxies that show a sign of AGN. The property that we use to identify AGN is the radio luminosity. If the radio luminosity of a radio source (L_{rad}) galaxy is $L_{rad} > 1 \times 10^{24}$ W/Hz, we consider it an AGN. This AGN luminosity threshold is adapted from Del Moro et al. 2013 where radio-excess sources amongst distant star-forming galaxies are selected from the GOODS-N (Great Observatories Origins Deep Survey- North) in search for any hidden AGN activity. In this paper radio-excess sources have radio luminosities typical of radio-loud AGNs, that is, with $L_{rad} > 1 \times 10^{24}$ W/Hz. Note that this is a fairly blunt approach because we might be cutting off some genuine, extreme star-forming galaxies, or including low luminosity AGNs. Unfortunately, given the data that we have nothing can be done to avoid this and so this is the best approach we have. From the sample of 1051 galaxies at the cluster redshift associated with a radio source, the number which were not associated with AGNs is 599 ($\sim 57\%$). Note that this is the number of sources used for the map before masking was done.

3.4.4 Projected Star Formation Density Map

To make our SFR/Area density map we first create a blank, square pixel map with the same dimensions and pixelisation as the WIRDS density map (see Section 3.2).

We add up the calculated SFR of the MeerKAT sources to a pixel in the map where those galaxies are found. We divide the integrated SFR by the area of each pixel. The SFR/Area projected density map is shown in Figure 3.10.

To enable a direct comparison between the SFR/Area and the number of galaxies found in each area of the image, we make a number density map of the galaxies associated with the cluster (see Figure 3.11) which shows the number density distribution of the 599 AGN-free galaxies.

One interesting thing we notice in Figure 3.10 is that the map shows a lower SFR density at regions B and D, however these regions have a high galaxy-number density (see Figure 3.11). This means that regions A-D have high number-density, but the star-forming activity at B and D appears rather hindered compared to A and C in Figure 3.10. Cores of clusters are not usually the sites of star formation, in fact they are the reverse. Therefore, it is not surprising that region D (enclosing the cluster center) is not showing a high SFR density.

3.5 Contour overlays

We create contours for each of the above density maps, that is, the WIRDS and SFR/Area density maps (Figures 3.4 and 3.10). To visually compare the features between the two density maps we overplot the contours from 3.4 onto 3.10, and vice versa.

3.5.1 WIRDS map overlaid with SFR/Area contours

The red SFR/Area contours show where the peaks in the SFR density are (see Figure 3.12). We notice that there is a peak SFR area at regions A and C.

3.5.2 SFR/Area map overlaid with WIRDS contours

In our SFR/Area density map overlaid with WIRDS projected galaxy density contours (shown in cyan in Figure 3.13) we notice that the galaxy density peaks fall within regions A, B and D. We also notice that besides C being one of the regions showing high SFRs (see Figure 3.12), it also shows to not have a corresponding high number density as we might have expected.

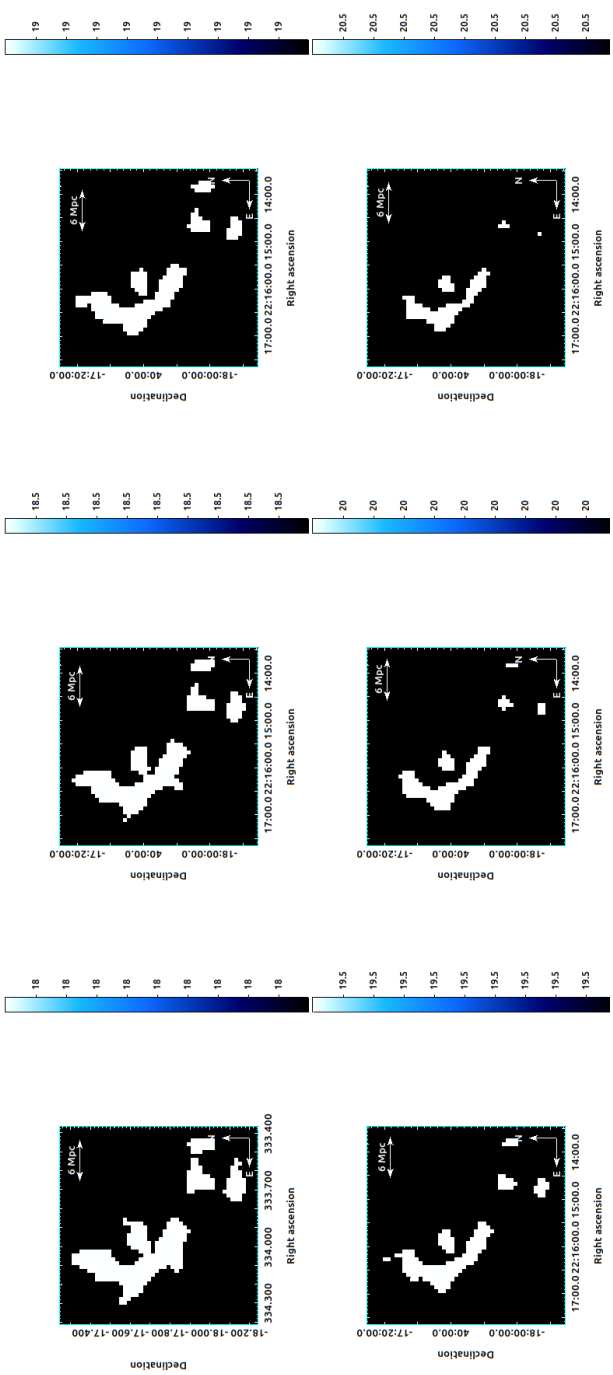

Figure 3.6: Comparison between the different thresholds on the WIRDS map used to outline the filament-like structure. The units of this image are in Mpc^{-2}.

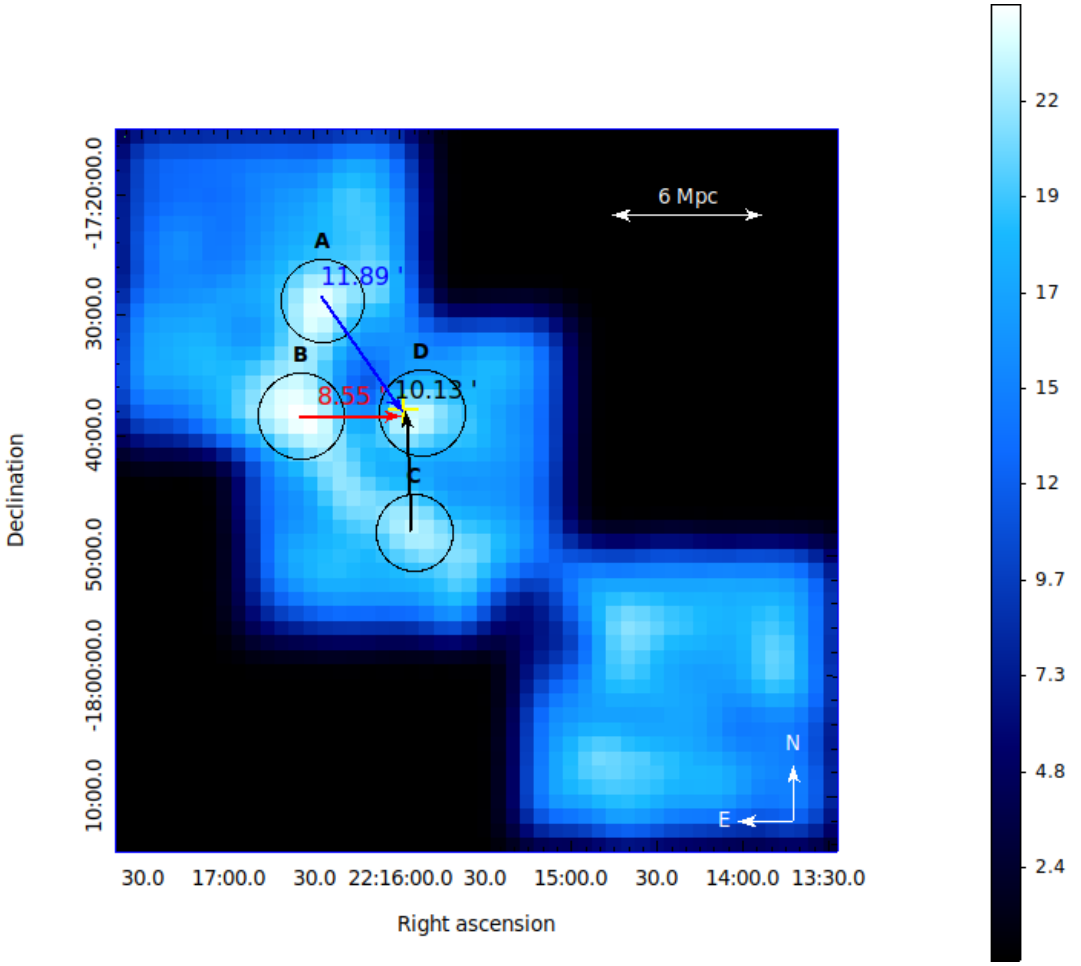

Figure 3.7: WIRDS density map showing the measured distances from regions A-C to the cluster center. The distances are represented by the blue, red and black vectors, respectively. The distances from the center of regions A, B and C from the cluster center is 11.89 ′, 8.55 ′ and 10.13 ′, which correspond to distances of 6.13 Mpc, 4.41 Mpc and 5.22 Mpc, respectively. The units of this image are in galaxies per square Mpc.

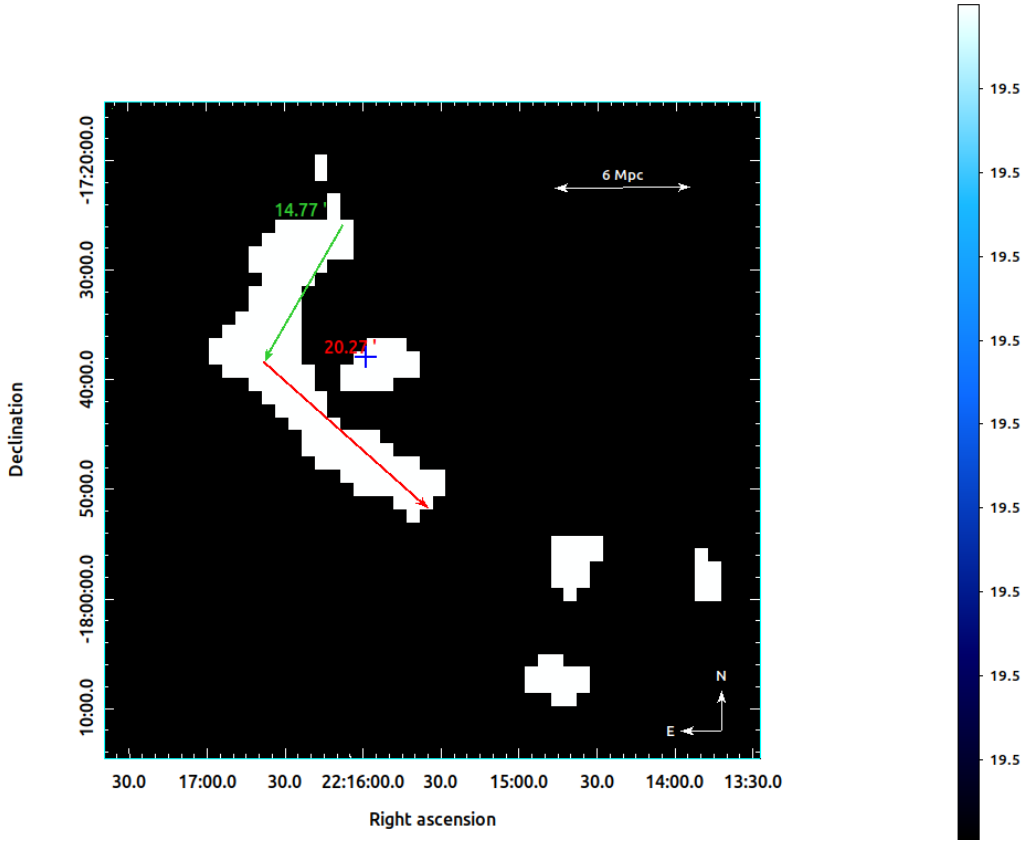

Figure 3.8: WIRDS density map of a pixel distribution with both the upper and lower scaling parameter limits set at 19.5 Mpc^{-2}. The blue and the red vector add to the length of the filament-like C-shaped structure. The blue and red vectors are 14.77 $'$ and 20.27 $'$ long, respectively, and add up to a length of 35.04 $'$. The cluster center coordinate position is shown by the blue "+".

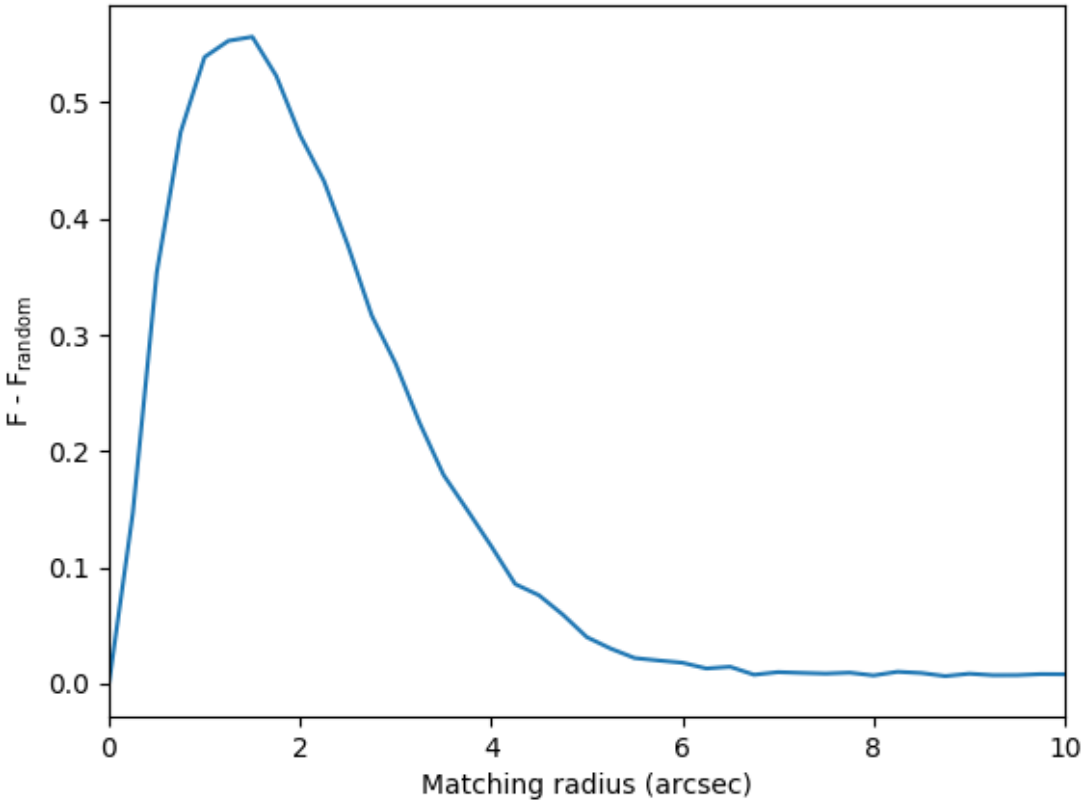

Figure 3.9: $F - F_{random}$ versus matching radius plot used to determine the best crossmatch radius (in $''$) between the MeerKAT radio source catalog and the WIRDS optical/infrared catalog, with the positions offset by $1''$.

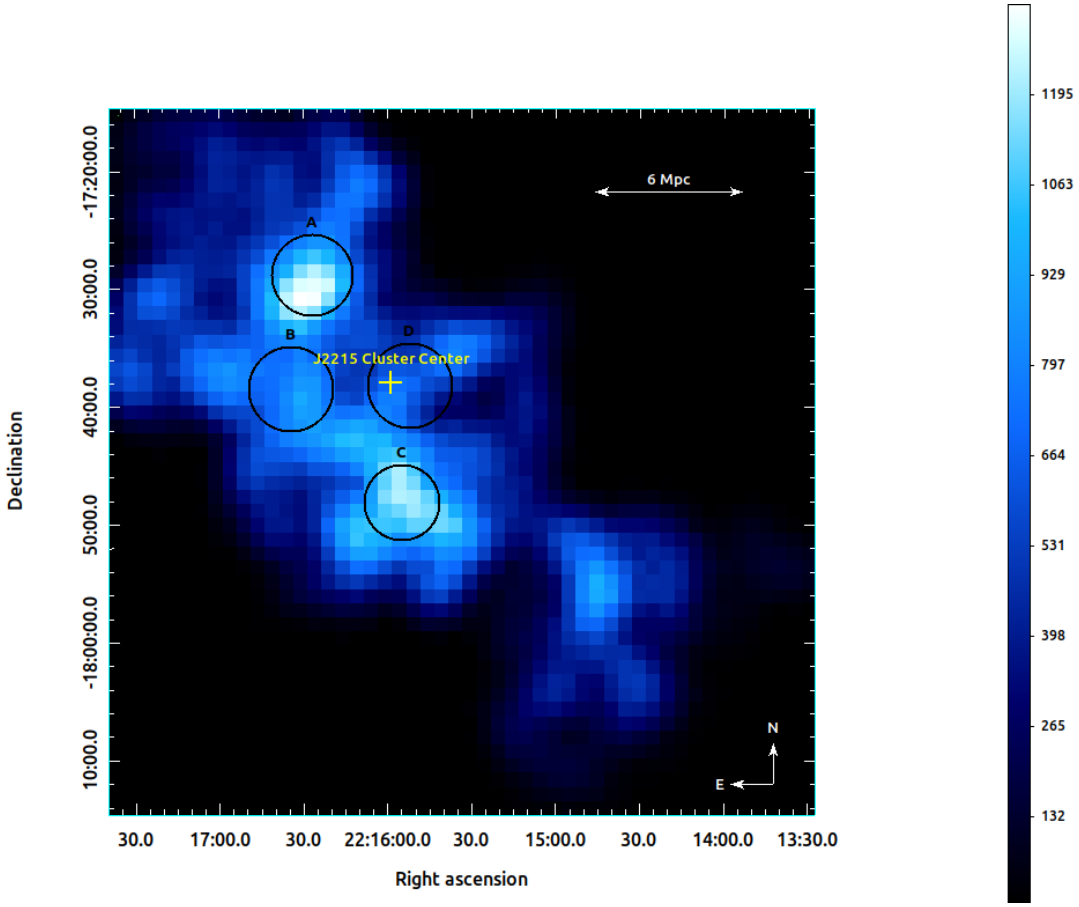

Figure 3.10: SFR/Area density map of the D4 field overlaid with regions A, B, C and D. The color units for this image are in $M_{\odot}yr^{-1}Mpc^{-2}$. The cluster center, indicated by the yellow "+", is at RA and Dec coordinates 22:15:58.5, -17:38:2.5.

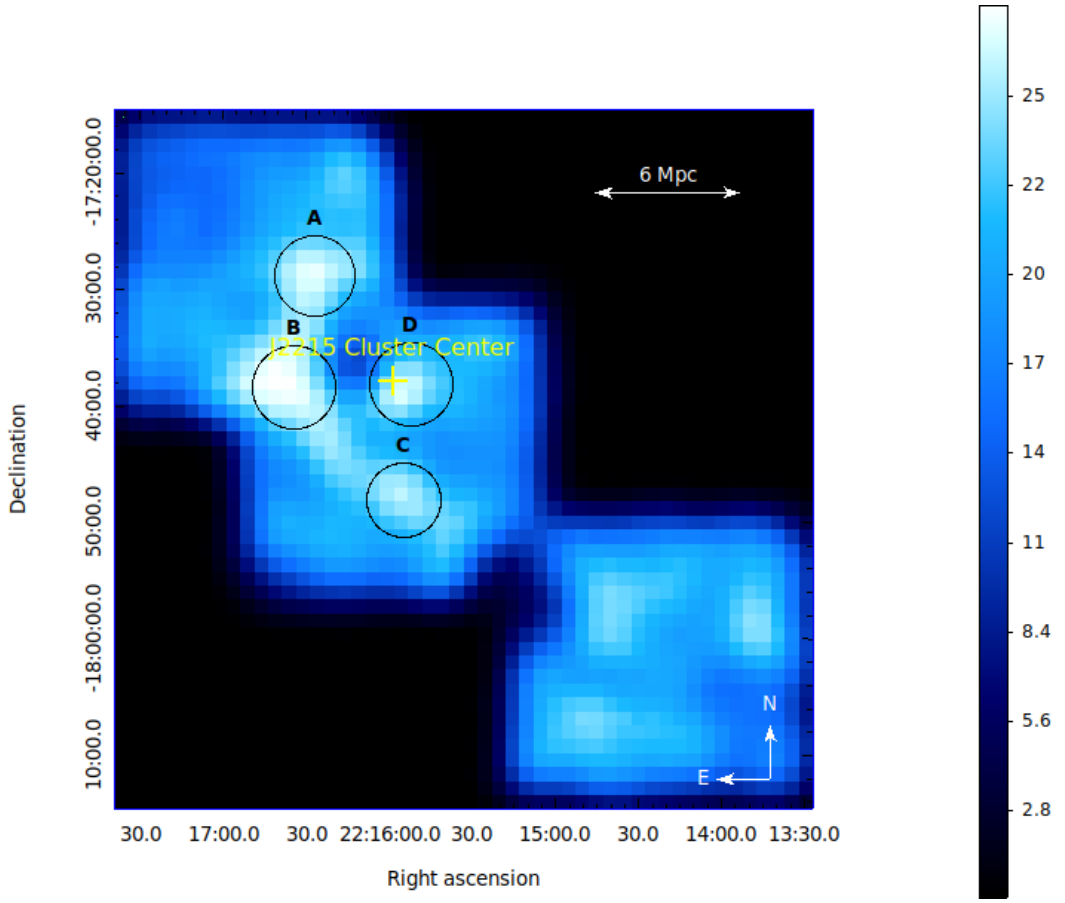

Figure 3.11: Number of galaxies at cluster redshift/Area density map (same sample as Figure 3.5) in the D4 field overlaid with the region outside of the WIRDS *Ks*-band region masked. Regions A, B, C and D are bounded within the black circles. The cluster center position is marked by the yellow "+". The color units for this image are in galaxies per square Mpc.

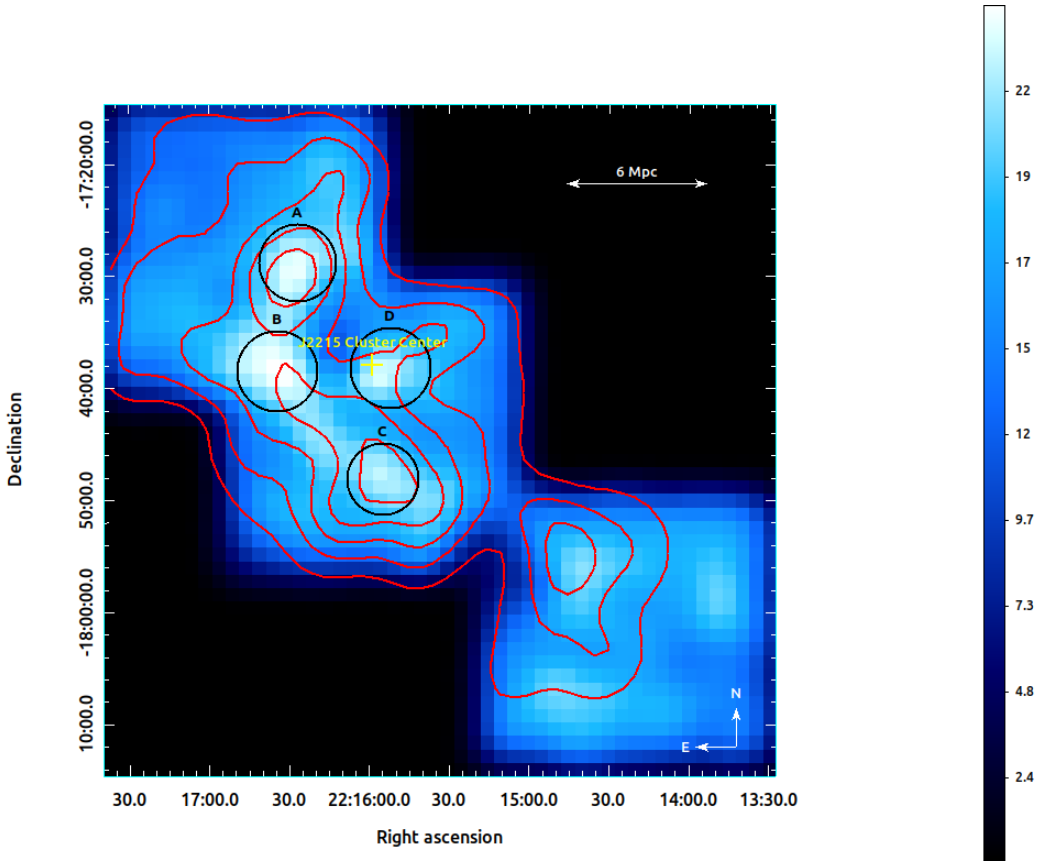

Figure 3.12: WIRDS density map overlaid with SFR/Area contours shown in red. The units of this image are in Mpc^{-2}. The contour levels are at 200, 400, 600, 800 and 1000 $\mathrm{M}_{\odot}\mathrm{yr}^{-1}\mathrm{Mpc}^{-2}$.

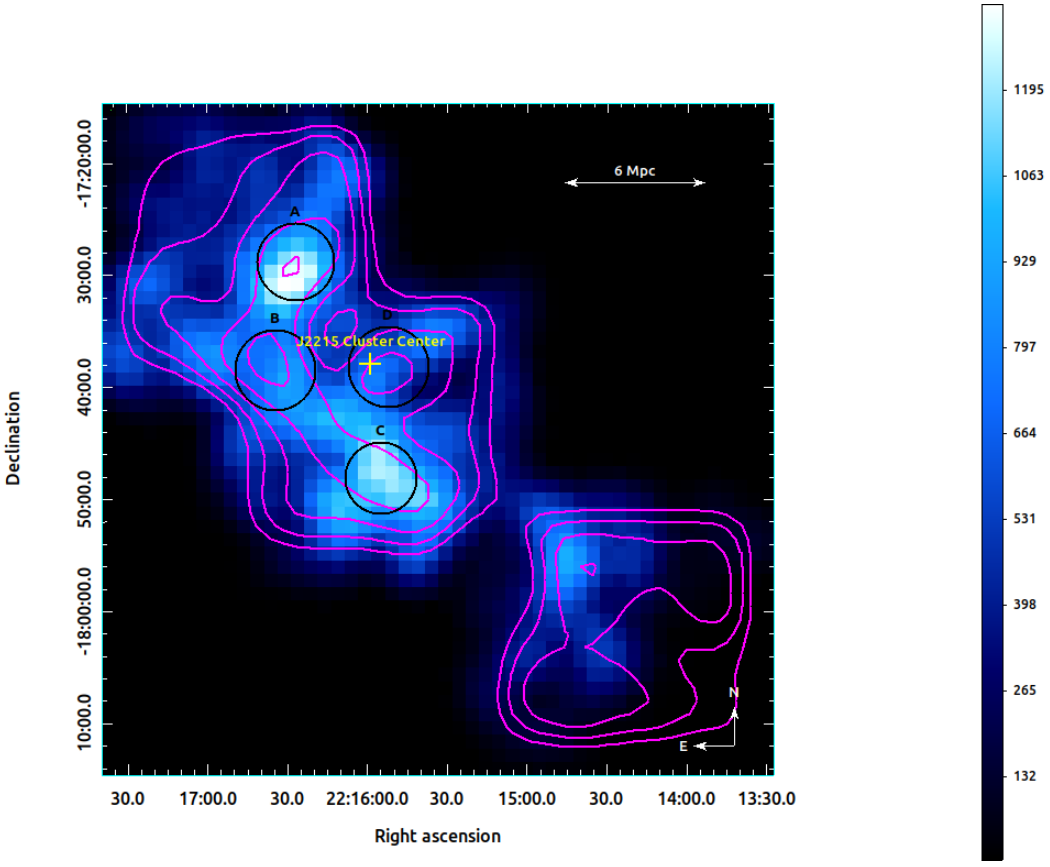

Figure 3.13: SFR/Area density map overlaid with WIRDS contours shown in magenta. The units of this image are in $M_{\odot}yr^{-1}Mpc^{-2}$. The contour levels show the projected galaxy density in galaxies per square Mpc at 13.0, 15.3, 17.5, 19.8 and 22.0.

Chapter 4

Discussion

According to studies that have been done, it has been shown that the J2215 cluster has a high star-forming core compared to clusters at lower redshifts (Hayashi et al., 2010). However, we would like to know whether this high star-forming activity also takes place in groups beyond the cluster's virial radius of 0.8 Mpc (Hilton et al., 2010). In this thesis we have traced some C-shaped filamentary-like structure around the young active J2215.9-1738 galaxy cluster at $z = 1.46$. The filament-like structure is ≈18.3 Mpc long and is located at ≈ 4.41 Mpc away from the cluster center when measured from the midpoint of the C-shape to the cluster center position. Within this filament there are three distinct groups (regions A, B and C), with a high galaxy density. Of the three, A and C have a high SFR density (see Figure 3.10) and are located ≈ 6.13 Mpc (≈ 7.66×R_{200}) and ≈ 5.22 Mpc (≈ 6.53×R_{200}) away from the cluster center, respectively (Figure 3.7).

4.1 Star-forming groups around J2215

From Figure 3.10 we notice that the SFR density at regions A and C is the most significant on the image. Regions A and C are approximately located 6.13 Mpc

and 5.22 Mpc away from the cluster center (see Figure 3.7). They are embedded at the ends of the C-shape filament. Hayashi et al. 2011 created contours using the local density, $\sum 5_{th}$, which is calculated using the area where the fifth nearest OII emitters are included. The OII emitters in Figure 4.1 show the tracings of regions A, B and C by the blue contours, which correspond to $\log\sum 5_{th} = 1.07$ Mpc^{-2} shown in the Hayashi et al. (2011) paper. From Figure 3.12, the SFR density for regions A and C is > 1000 M$_\odot$yr^{-1}Mpc^{-2}.

4.2 Filament-like structure traced by regions A, B and C, and cluster center by D

The filament-like large scale structure that we see in Figure 3.8 is located from the east to the south of cluster. This agrees with the results of Hayashi et al. (2011) which also locates a filament structure of OII emitters surrounding the cluster at a similar position (see Figure 4.1), where the OII emitters also seem to trace the cluster center (region D). However, we do note that the filament-structure that we detected extends further north of the cluster than seen in Figure 4.1 from Hayashi et al. (2011). This filament is the largest structure showing signs of star-formation at $z = 1.46$.

The filament is made up of regions A-C. When we measure the C-shaped filament-like structure, we estimate that it is ≈ 18.07 Mpc long when measured end-to-end (see Figure 3.8). Furthermore, we determine the distances of regions A, B and C away from the cluster center. We estimated these distances using the measuring vector tool on `DS9`. The lengths measured from the center of each region to the cluster center position (see Figure 3.7) is approximately ≈ 6.13 Mpc, 4.41 Mpc and 5.22 Mpc, respectively.

We also notice a SFR property of the filament seen in Figure 3.12. Fig-

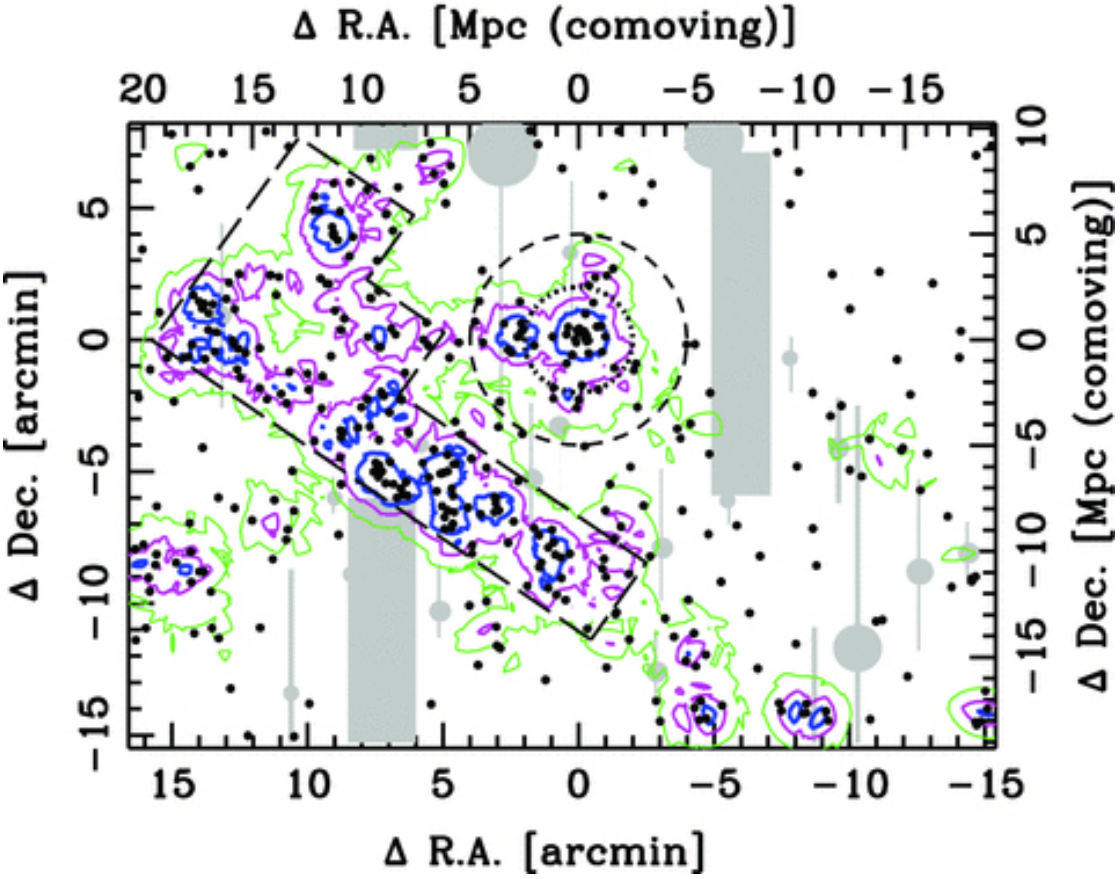

Figure 4.1: A celestial distribution of 380 OII emitters at z ∼1 .46 in and around the XCS2215 cluster from the Hayashi et al. 2011 paper. North is up, and east is to the left. The horizontal and vertical axes show the coordinates with respect to the cluster centre. Black dots show the OII emitters, and grey regions show the masked areas around bright stars which were masked. The cluster core region is defined by a dotted-line circle with a radius of 2 arcmin, while the outskirts region is defined as a ring with a width of 2 arcmin between the dotted and broken-line circles. Filament region shown by the long-dashed lines and is defined to cover the prominent structure of the OII emitters. The rest of the area is defined as the field. The blue, magenta and green contours show the local density of $\log\sum 5_{th}[\mathrm{Mpc}^{-2}]$ = 1.07, 0.72 and 0.39, respectively, where $\sum 5_{th}$ is a local density parameter used by Hayashi et al. 2011 to define the environment. It is calculated using the area where the fifth nearest OII emitters are included. Source: (Hayashi et al., 2011)

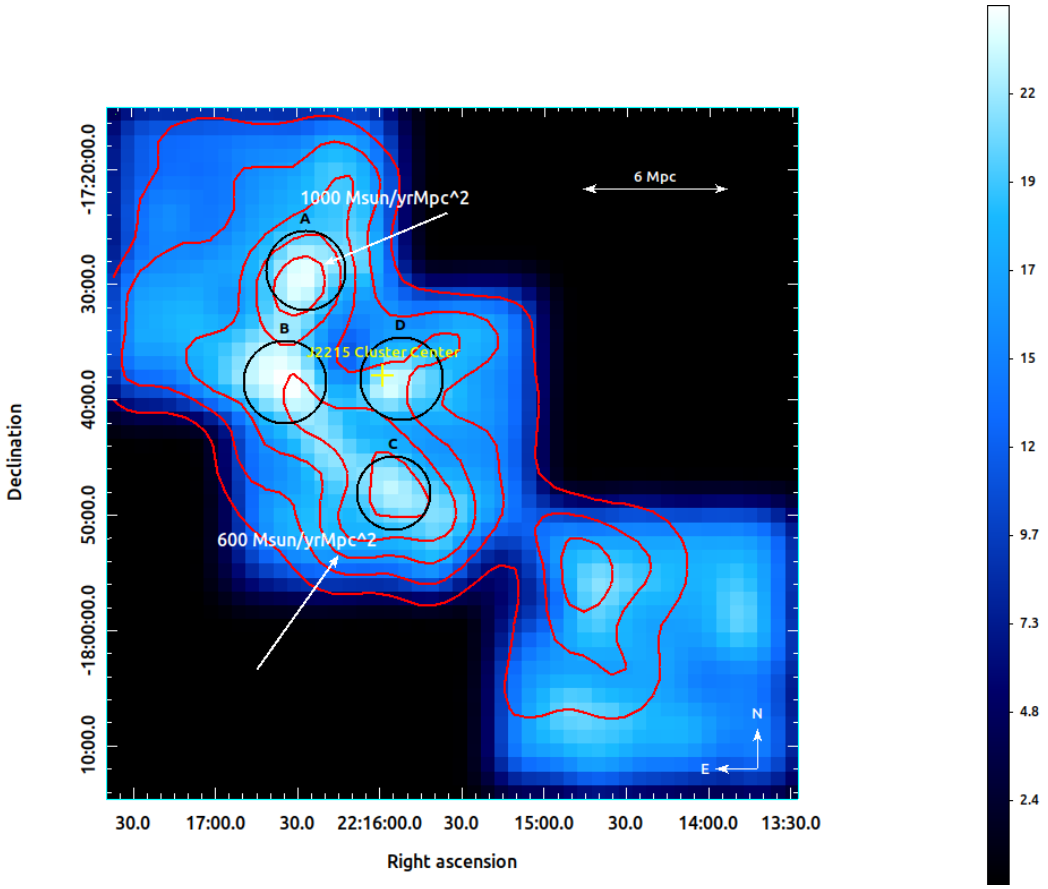

Figure 4.2: WIRDS density map overlaid with SFR/Area contours shown in red. Note that this is a repeat of Figures 3.5 and 3.12 with only the white arrows pointing at the peaks. The units of this image are in Mpc^{-2}. The contour levels are at 200, 400, 600, 800 and 1000 $\mathrm{M}_{\odot}\mathrm{yr}^{-1}\mathrm{Mpc}^{-2}$. The 600 and 1000 $\mathrm{M}_{\odot}\mathrm{yr}^{-1}\mathrm{Mpc}^{-2}$ contour levels are pointed at by white arrows.

ure 4.2 reveals that the filament falls within the contour level SFR/Area = 600 $M_{\odot}yr^{-1}Mpc^{-2}$ (see white arrow in Figure 4.2). This indicates evidence of a high intensity star formation activity in this filament.

Furthermore, regions A and C at each end of the C-shape indicate an existence of star-formation activity which exceeds 1000 $M_{\odot}yr^{-1}Mpc^{-2}$ (see contour peaks in Figure 4.2 at A and C). All the abovementioned results are in quantitative agreement with the optical/OII narrowband study by Hayashi et al. 2011. To confirm our detection of star-forming galaxies in the filament-like structure near J2215 with MeerKAT will require further follow-up observations such as obtaining the optical spectroscopy of the MeerKAT radio sources identified within the "filament".

Chapter 5

Conclusion

We have explored the SFRs within groups and filamentary-like stuctures surrounding the cluster J2215.9-1738 at z= 1.46 using high-resolution radio data from MeerKAT and near-infrared/optical observations from the WIRCam Deep Survey. This is the first study of dust-unobscured SFRs since we used the radio continuum to trace star forming galaxies, unlike previous studies which have done so using OII emission luminosities (e.g. Hayashi et al., 2010). Our results have shown that the high star-formation properties do extend into J2215's surroundings. We summarize our findings below:

1. A filament-like structure $\approx$ 18.07 Mpc long is located from the east to the south of the cluster. The filament-like structure center is $\approx$ 4.41 Mpc away from the cluster center. Although using different data, our filament agrees well with the filament-like structure seen in Hayashi et al. (2011) who used Subaru/MOIRCS data (OII emitters) to trace the filament-like structure shape.

2. There are star forming galaxies in our filament. The filament-like structure roughly consists of three significant groups (regions A-C) that have a significant number of galaxies per square Mpc compared to the rest of the image (Figure 3.8). However, only regions A and C have a significant SFR per square Mpc within the

filament-like structure compared to region B. The SFR density seen in regions A and C of the filament-like structure is quantitatively higher than the SFR density within the virial radius (Figure 3.10). From Figure 3.12, the SFR density for regions A and C is > 1000 $M_{\odot}yr^{-1}Mpc^{-2}$ making this a lower limit of the SFR within the filament.

5.1 Limitations and/or uncertainties in the presented research

In this research we used photometric redshifts that were estimated using the SED template-fitting method through the EAZY algorithm. As already mentioned in Section 3.1.3, some photo-z estimates for some galaxies may deviate from the true value because the galaxy might have a spectral shape that isn't covered by the chosen template set. Secondly, our use of the AGN luminosity threshold from Del Moro et al. 2013 where radio sources with with $L_{rad} > 1 \times 10^{24}$ W/Hz are considered AGNs may not be bullet proof. It may be that did not identify all the real AGNs in our sample, therefore leading to higher estimations of SFRs.

5.2 Future work

In this thesis we used MeerKAT radio emission to determine the SFRs of the galaxies at the cluster redshift. For future work, we need to do optical/IR spectroscopy of these MeerKAT sources via photo-zs to confirm them as star-forming galaxies at z$\approx$1.46, and to rule out any AGN contamination.

Bibliography

Abell, G. O., 1958, 'The Distribution of Rich Clusters of Galaxies.', *The Astrophysical Journal Supplement Series*, 3, 211.

Asad, K. M. B., Girard, J. N., de Villiers, M., Ansah-Narh, T., Iheanetu, K., Smirnov, O., Santos, M. G., Lehmensiek, R., Jonas, J., de Villiers, D. I. L., Thorat, K., Hugo, B., Makhathini, S., Jozsa, G. I. G., Sirothia, S. K., 2021, 'Primary beam effects of radio astronomy antennas - II. Modelling MeerKAT L-band beams', *MNRAS*, 502 (2), 2970–2983.

Beisbart, C., 2009, 'Can we justifiably assume the cosmological principle in order to break model underdetermination in cosmology?', *Journal for General Philosophy of Science*, 40, 175–205.

Bell, E. F., 2003, 'Estimating Star Formation Rates from Infrared and Radio Luminosities: The Origin of the Radio-Infrared Correlation', *ApJ*, 586 (2), 794–813.

Benítez, N., 2000, 'Bayesian Photometric Redshift Estimation', *ApJ*, 536 (2), 571–583.

Bielby, R., Hudelot, P., McCracken, H. J., Ilbert, O., Daddi, E., Le Fèvre, O., Gonzalez-Perez, V., Kneib, J. P., Marmo, C., Mellier, Y., Salvato, M., Sanders, D. B., Willott, C. J., 2012, 'The WIRCam Deep Survey. I. Counts, colours, and

mass-functions derived from near-infrared imaging in the CFHTLS deep fields', *A&A*, 545, A23.

Bielby, R. M., Finoguenov, A., Tanaka, M., McCracken, H. J., Daddi, E., Hudelot, P., Ilbert, O., Kneib, J. P., Le Fèvre, O., Mellier, Y., Nandra, K., Petitjean, P., Srianand, R., Stalin, C. S., Willott, C. J., 2010, 'The wircam deep infrared cluster survey-i. groups and clusters at ≥ 1.1', *A&A*, 523, A66.

Blanton, M. R., Roweis, S., 2007, 'K-Corrections and Filter Transformations in the Ultraviolet, Optical, and Near-Infrared', *The Astronomical Journal*, 133 (2), 734–754.

Bolzonella, M., Miralles, J. M., Pelló, R., 2000, 'Photometric redshifts based on standard SED fitting procedures', *A&A*, 363, 476–492.

Bond, J. R., Efstathiou, G., 1984, 'Cosmic background radiation anisotropies in universes dominated by nonbaryonic dark matter', *The Astrophysical Journal*, 285, L45–L48.

Boylan-Kolchin, M., Springel, V., White, S. D. M., Jenkins, A., Lemson, G., 2009, 'Resolving cosmic structure formation with the Millennium-II Simulation', *MNRAS*, 398 (3), 1150–1164.

Brammer, G. B., van Dokkum, P. G., Coppi, P., 2008, 'EAZY: A Fast, Public Photometric Redshift Code', *ApJ*, 686 (2), 1503–1513.

Brodwin, M., Stanford, S. A., Gonzalez, A. H., Zeimann, G. R., Snyder, G. F., Mancone, C. L., Pope, A., Eisenhardt, P. R., Stern, D., Alberts, S., Ashby, M. L. N., Brown, M. J. I., Chary, R. R., Dey, A., Galametz, A., Gettings, D. P., Jannuzi, B. T., Miller, E. D., Moustakas, J., Moustakas, L. A., 2013, 'The Era of Star Formation in Galaxy Clusters', *ApJ*, 779 (2), 138.

Carlberg, R. G., Yee, H. K. C., Ellingson, E., Morris, S. L., Abraham, R., Gravel, P., Pritchet, C. J., Smecker-Hane, T., Hartwick, F. D. A., Hesser, J. E., Hutchings, J. B., Oke, J. B., 1997, 'The Dynamical Equilibrium of Galaxy Clusters', *The Astrophysical Journal*, 476 (1), L7–L10.

Cautun, M., van de Weygaert, R., Jones, B. J. T., 2013, 'NEXUS: tracing the cosmic web connection', *MNRAS*, 429 (2), 1286–1308.

Cautun, M., van de Weygaert, R., Jones, B. J. T., Frenk, C. S., 2016, 'Understanding the cosmic web', 308, 47–56.

Coleman, G. D., Wu, C. C., Weedman, D. W., 1980, 'Colors and magnitudes predicted for high redshift galaxies.', *The Astrophysical Journal Supplement Series*, 43, 393–416.

Condon, J. J., 1992, 'Radio emission from normal galaxies.', *Annual Reviews in Astronomy & Astrophysics*, 30, 575–611.

Csabai, I., Budavári, T., Connolly, A. J., Szalay, A. S., Győry, Z., Benítez, N., Annis, J., Brinkmann, J., Eisenstein, D., Fukugita, M., Gunn, J., Kent, S., Lupton, R., Nichol, R. C., Stoughton, C., 2003, 'The Application of Photometric Redshifts to the SDSS Early Data Release', *The Astronomical Journal*, 125 (2), 580–592.

Del Moro, A., Alexander, D. M., Mullaney, J. R., Daddi, E., Pannella, M., Bauer, F. E., Pope, A., Dickinson, M., Elbaz, D., Barthel, P. D., Garrett, M. A., Brandt, W. N., Charmandaris, V., Chary, R. R., Dasyra, K., Gilli, R., Hickox, R. C., Hwang, H. S., Ivison, R. J., Juneau, S., Le Floc'h, E., Luo, B., Morrison, G. E., Rovilos, E., Sargent, M. T., Xue, Y. Q., 2013, 'GOODS-Herschel: radio-excess signature of hidden AGN activity in distant star-forming galaxies', *A&A*, 549, A59.

Dressler, A., 1980, 'Galaxy morphology in rich clusters: implications for the formation and evolution of galaxies.', *ApJ*, 236, 351–365.

Dressler, A., Oemler, Augustus, J., Couch, W. J., Smail, I., Ellis, R. S., Barger, A., Butcher, H., Poggianti, B. M., Sharples, R. M., 1997, 'Evolution since z = 0.5 of the Morphology-Density Relation for Clusters of Galaxies', *ApJ*.

Gomes, Z., Jarvis, M. J., Almosallam, I. A., Roberts, S. J., 2018, 'Improving photometric redshift estimation using GPZ: size information, post processing, and improved photometry', *MNRAS*, 475 (1), 331–342.

Gunn, J. E., Gott, J. Richard, I., 1972, 'On the Infall of Matter Into Clusters of Galaxies and Some Effects on Their Evolution', *ApJ*, 176, 1.

Hayashi, M., Kodama, T., Kohno, K., Yamaguchi, Y., Tadaki, K.-i., Hatsukade, B., Koyama, Y., Shimakawa, R., Tamura, Y., Suzuki, T. L., 2017, 'Evolutionary Phases of Gas-rich Galaxies in a Galaxy Cluster at z = 1.46', *The Astrophysical Journal*, 841 (2), L21.

Hayashi, M., Kodama, T., Koyama, Y., Tadaki, K.-I., Tanaka, I., 2011, 'Properties of star-forming galaxies in a cluster and its surrounding structure at z=1.46', *MNRAS*, 415 (3), 2670–2687.

Hayashi, M., Kodama, T., Koyama, Y., Tanaka, I., Shimasaku, K., Okamura, S., 2010, 'High star formation activity in the central region of a distant cluster at z = 1.46', *MNRAS*, 402 (3), 1980–1990.

Heywood, I., 2020. oxkat: Semi-automated imaging of MeerKAT observations. Astrophysics Source Code Library, record ascl:2009.003.

Hilton, M., Collins, C. A., Stanford, S. A., Lidman, C., Dawson, K. S., Davidson, M., Kay, S. T., Liddle, A. R., Mann, R. G., Miller, C. J., Nichol, R. C., Romer,

A. K., Sabirli, K., Viana, P. T. P., West, M. J., 2007, 'The XMM Cluster Survey: The Dynamical State of XMMXCS J2215.9-1738 at z = 1.457', *ApJ*, 670 (2), 1000–1009.

Hilton, M., Lloyd-Davies, E., Stanford, S. A., Stott, J. P., Collins, C. A., Romer, A. K., Hosmer, M., Hoyle, B., Kay, S. T., Liddle, A. R., Mehrtens, N., Miller, C. J., Sahlén, M., Viana, P. T. P., 2010, 'The XMM Cluster Survey: Active Galactic Nuclei and Starburst Galaxies in XMMXCS J2215.9-1738 at z = 1.46', *ApJ*, 718 (1), 133–147.

Hilton, M., Stanford, S. A., Stott, J. P., Collins, C. A., Hoyle, B., Davidson, M., Hosmer, M., Kay, S. T., Liddle, A. R., Lloyd-Davies, E., Mann, R. G., Mehrtens, N., Miller, C. J., Nichol, R. C., Romer, A. K., Sabirli, K., Sahlén, M., Viana, P. T. P., West, M. J., Barbary, K., Dawson, K. S., Meyers, J., Perlmutter, S., Rubin, D., Suzuki, N., 2009, 'The XMM Cluster Survey: Galaxy Morphologies and the Color-Magnitude Relation in XMMXCS J2215.9 - 1738 at z = 1.46', *ApJ*, 697 (1), 436–451.

Ilbert, O., Arnouts, S., McCracken, H. J., Bolzonella, M., Bertin, E., Le Fèvre, O., Mellier, Y., Zamorani, G., Pellò, R., Iovino, A., Tresse, L., Le Brun, V., Bottini, D., Garilli, B., Maccagni, D., Picat, J. P., Scaramella, R., Scodeggio, M., Vettolani, G., Zanichelli, A., Adami, C., Bardelli, S., Cappi, A., Charlot, S., Ciliegi, P., Contini, T., Cucciati, O., Foucaud, S., Franzetti, P., Gavignaud, I., Guzzo, L., Marano, B., Marinoni, C., Mazure, A., Meneux, B., Merighi, R., Paltani, S., Pollo, A., Pozzetti, L., Radovich, M., Zucca, E., Bondi, M., Bongiorno, A., Busarello, G., de La Torre, S., Gregorini, L., Lamareille, F., Mathez, G., Merluzzi, P., Ripepi, V., Rizzo, D., Vergani, D., 2006, 'Accurate photometric redshifts for the CFHT legacy survey calibrated using the VIMOS VLT deep survey', *A&A*, 457 (3), 841–856.

Kauffmann, G., White, S. D. M., Heckman, T. M., Ménard, B., Brinchmann, J., Charlot, S., Tremonti, C., Brinkmann, J., 2004, 'The environmental dependence of the relations between stellar mass, structure, star formation and nuclear activity in galaxies', *MNRAS*, 353 (3), 713–731.

Kennicutt, Robert C., J., 1998, 'Star Formation in Galaxies Along the Hubble Sequence', *Annual Reviews in Astronomy & Astrophysics*, 36, 189–232.

Kennicutt, Robert C., J., Tamblyn, P., Congdon, C. E., 1994, 'Past and Future Star Formation in Disk Galaxies', *ApJ*, 435, 22.

Kinney, A. L., Calzetti, D., Bohlin, R. C., McQuade, K., Storchi-Bergmann, T., Schmitt, H. R., 1996, 'Template Ultraviolet to Near-Infrared Spectra of Star-forming Galaxies and Their Application to K-Corrections', *ApJ*, 467, 38.

Klutse, D. Y., Hilton, M., Heywood, I., in prep., 'Meerkat observation : Star formation rates and galaxy morphology studies within the core of the xmmxcs j2215.9-1738 galaxy cluster'.

Leitherer, C., Heckman, T. M., 1995, 'Synthetic Properties of Starburst Galaxies', *The Astrophysical Journal Supplement Series*, 96, 9.

Libeskind, N. I., van de Weygaert, R., Cautun, M., Falck, B., Tempel, E., Abel, T., Alpaslan, M., Aragón-Calvo, M. A., Forero-Romero, J. E., Gonzalez, R., Gottlöber, S., Hahn, O., Hellwing, W. A., Hoffman, Y., Jones, B. J. T., Kitaura, F., Knebe, A., Manti, S., Neyrinck, M., Nuza, S. E., Padilla, N., Platen, E., Ramachandra, N., Robotham, A., Saar, E., Shandarin, S., Steinmetz, M., Stoica, R. S., Sousbie, T., Yepes, G., 2018, 'Tracing the cosmic web', *MNRAS*, 473 (1), 1195–1217.

Liddle, A. R., 2015, 'An introduction to modern cosmology, Third Edition'.

Lloyd-Davies, E. J., Romer, A. K., Mehrtens, N., Hosmer, M., Davidson, M., Sabirli, K., Mann, R. G., Hilton, M., Liddle, A. R., Viana, P. T. P., Campbell, H. C., Collins, C. A., Dubois, E. N., Freeman, P., Harrison, C. D., Hoyle, B., Kay, S. T., Kuwertz, E., Miller, C. J., Nichol, R. C., Sahlén, M., Stanford, S. A., Stott, J. P., 2011, 'The XMM Cluster Survey: X-ray analysis methodology', *MNRAS*, 418 (1), 14–53.

Ma, C. J., Smail, I., Swinbank, A. M., Simpson, J. M., Thomson, A. P., Chen, C. C., Danielson, A. L. R., Hilton, M., Tadaki, K., Stott, J. P., Kodama, T., 2015, 'Dusty Starbursts and the Formation of Elliptical Galaxies: A SCUBA-2 Survey of a z = 1.46 Cluster', *ApJ*, 806 (2), 257.

Madau, P., Pozzetti, L., Dickinson, M., 1998, 'The Star Formation History of Field Galaxies', *ApJ*, 498 (1), 106–116.

Mas-Hesse, J. M., 1991. Evolutionary synthesis of the radio and far infrared emission in starbursts.

Massey, R., 2008, 'Viewing dark matter with weak gravitational lensing from HST', In: Baryshev, Y. V., Taganov, I. N., Teerikorpi, P. (Eds.), Problems of Practical Cosmology, Volume 1, Vol. 1, pp. 41–49.

Moore, B., Katz, N., Lake, G., Dressler, A., Oemler, A., 1996, 'Galaxy harassment and the evolution of clusters of galaxies', *Nature*, 379 (6566), 613–616.

Moore, B., Lake, G., Katz, N., 1998, 'Morphological Transformation from Galaxy Harassment', *ApJ*, 495 (1), 139–151.

Muzzin, A., Wilson, G., Yee, H. K. C., Gilbank, D., Hoekstra, H., Demarco, R., Balogh, M., van Dokkum, P., Franx, M., Ellingson, E., Hicks, A., Nantais, J., Noble, A., Lacy, M., Lidman, C., Rettura, A., Surace, J., Webb, T., 2012,

'The Gemini Cluster Astrophysics Spectroscopic Survey (GCLASS): The Role of Environment and Self-regulation in Galaxy Evolution at z ~1', *ApJ*, 746 (2), 188.

Nelson, D., Pillepich, A., Genel, S., Vogelsberger, M., Springel, V., Torrey, P., Rodriguez-Gomez, V., Sijacki, D., Snyder, G. F., Griffen, B., Marinacci, F., Blecha, L., Sales, L., Xu, D., Hernquist, L., 2015, 'The illustris simulation: Public data release', *Astronomy and Computing*, 13, 12–37.

Pearson, W. J., Wang, L., Alpaslan, M., Baldry, I., Bilicki, M., Brown, M. J. I., Grootes, M. W., Holwerda, B. W., Kitching, T. D., Kruk, S., van der Tak, F. F. S., 2019, 'Effect of galaxy mergers on star-formation rates', *A&A*, 631, A51.

Peebles, P. J. E., 1982, 'Large-scale background temperature and mass fluctuations due to scale-invariant primeval perturbations', *The Astrophysical Journal*, 263, L1–L5.

Peng, Y., Maiolino, R., Cochrane, R., 2015, 'Strangulation as the primary mechanism for shutting down star formation in galaxies', *Nature*, 521 (7551), 192–195.

Perivolaropoulos, L., Skara, F., 2022, 'Challenges for ΛCDM: An update', *New Astronomy Review*, 95, 101659.

Perlmutter, S., Aldering, G., Boyle, B. J., Castro, P. G., Couch, W. J., Deustua, S., Fabbro, S., Ellis, R. S., Filippenko, A. V., Fruchter, A., Goldhaber, G., Goobar, A., Groom, D. E., Hook, I. M., Irwin, M., Kim, A. G., Kim, M. Y., Knop, R. A., Lee, J. C., Matheson, T., McMahon, R. G., Newberg, H. J. M., Lidman, C., Nugent, P., Nunes, N. J., Pain, R., Panagia, N., Pennypacker, C. R., Quimby, R., Ruiz-Lapuente, P., Schaefer, B., Walton, N., Supernova

Cosmology Project, 1998, 'Measurements of Omega and Lambda from 42 High-Redshift Supernovae', In: Paul, J., Montmerle, T., Aubourg, E. (Eds.), 19th Texas Symposium on Relativistic Astrophysics and Cosmology, p. 146.

Planck Collaboration, Ade, P. A. R., Aghanim, N., Armitage-Caplan, C., Arnaud, M., Ashdown, M., Atrio-Barandela, F., Aumont, J., Baccigalupi, C., Banday, A. J., Barreiro, R. B., Bartlett, J. G., Battaner, E., Benabed, K., Benoît, A., Benoit-Lévy, A., Bernard, J. P., Bersanelli, M., Bielewicz, P., Bobin, J., Bock, J. J., Bonaldi, A., Bond, J. R., Borrill, J., Bouchet, F. R., Bridges, M., Bucher, M., Burigana, C., Butler, R. C., Calabrese, E., Cappellini, B., Cardoso, J. F., Catalano, A., Challinor, A., Chamballu, A., Chary, R. R., Chen, X., Chiang, H. C., Chiang, L. Y., Christensen, P. R., Church, S., Clements, D. L., Colombi, S., Colombo, L. P. L., Couchot, F., Coulais, A., Crill, B. P., Curto, A., Cuttaia, F., Danese, L., Davies, R. D., Davis, R. J., de Bernardis, P., de Rosa, A., de Zotti, G., Delabrouille, J., Delouis, J. M., Désert, F. X., Dickinson, C., Diego, J. M., Dolag, K., Dole, H., Donzelli, S., Doré, O., Douspis, M., Dunkley, J., Dupac, X., Efstathiou, G., Elsner, F., Enßlin, T. A., Eriksen, H. K., Finelli, F., Forni, O., Frailis, M., Fraisse, A. A., Franceschi, E., Gaier, T. C., Galeotta, S., Galli, S., Ganga, K., Giard, M., Giardino, G., Giraud-Héraud, Y., Gjerløw, E., González-Nuevo, J., Górski, K. M., Gratton, S., Gregorio, A., Gruppuso, A., Gudmundsson, J. E., Haissinski, J., Hamann, J., Hansen, F. K., Hanson, D., Harrison, D., Henrot-Versillé, S., Hernández-Monteagudo, C., Herranz, D., Hildebrandt, S. R., Hivon, E., Hobson, M., Holmes, W. A., Hornstrup, A., Hou, Z., Hovest, W., Huffenberger, K. M., Jaffe, A. H., Jaffe, T. R., Jewell, J., Jones, W. C., Juvela, M., Keihänen, E., Keskitalo, R., Kisner, T. S., Kneissl, R., Knoche, J., Knox, L., Kunz, M., Kurki-Suonio, H., Lagache, G., Lähteenmäki, A., Lamarre, J. M., Lasenby, A., Lattanzi, M., Laureijs, R. J., Lawrence, C. R., Leach, S., Leahy, J. P., Leonardi, R., León-Tavares, J., Lesgourgues, J., Lewis,

A., Liguori, M., Lilje, P. B., Linden-Vørnle, M., López-Caniego, M., Lubin, P. M., Macías-Pérez, J. F., Maffei, B., Maino, D., Mandolesi, N., Maris, M., Marshall, D. J., Martin, P. G., Martínez-González, E., Masi, S., Massardi, M., Matarrese, S., Matthai, F., Mazzotta, P., Meinhold, P. R., Melchiorri, A., Melin, J. B., Mendes, L., Menegoni, E., Mennella, A., Migliaccio, M., Millea, M., Mitra, S., Miville-Deschênes, M. A., Moneti, A., Montier, L., Morgante, G., Mortlock, D., Moss, A., Munshi, D., Murphy, J. A., Naselsky, P., Nati, F., Natoli, P., Netterfield, C. B., Nørgaard-Nielsen, H. U., Noviello, F., Novikov, D., Novikov, I., O'Dwyer, I. J., Osborne, S., Oxborrow, C. A., Paci, F., Pagano, L., Pajot, F., Paladini, R., Paoletti, D., Partridge, B., Pasian, F., Patanchon, G., Pearson, D., Pearson, T. J., Peiris, H. V., Perdereau, O., Perotto, L., Perrotta, F., Pettorino, V., Piacentini, F., Piat, M., Pierpaoli, E., Pietrobon, D., Plaszczynski, S., Platania, P., Pointecouteau, E., Polenta, G., Ponthieu, N., Popa, L., Poutanen, T., Pratt, G. W., Prézeau, G., Prunet, S., Puget, J. L., Rachen, J. P., Reach, W. T., Rebolo, R., Reinecke, M., Remazeilles, M., Renault, C., Ricciardi, S., Riller, T., Ristorcelli, I., Rocha, G., Rosset, C., Roudier, G., Rowan-Robinson, M., Rubiño-Martín, J. A., Rusholme, B., Sandri, M., Santos, D., Savelainen, M., Savini, G., Scott, D., Seiffert, M. D., Shellard, E. P. S., Spencer, L. D., Starck, J. L., Stolyarov, V., Stompor, R., Sudiwala, R., Sunyaev, R., Sureau, F., Sutton, D., Suur-Uski, A. S., Sygnet, J. F., Tauber, J. A., Tavagnacco, D., Terenzi, L., Toffolatti, L., Tomasi, M., Tristram, M., Tucci, M., Tuovinen, J., Türler, M., Umana, G., Valenziano, L., Valiviita, J., Van Tent, B., Vielva, P., Villa, F., Vittorio, N., Wade, L. A., Wandelt, B. D., Wehus, I. K., White, M., White, S. D. M., Wilkinson, A., Yvon, D., Zacchei, A., Zonca, A., 2014, 'Planck 2013 results. XVI. Cosmological parameters', *A&A*, 571, A16.

Planck Collaboration, Aghanim, N., Akrami, Y., Ashdown, M., Aumont, J., Baccigalupi, C., Ballardini, M., Banday, A. J., Barreiro, R. B., Bartolo, N., Basak,

S., Battye, R., Benabed, K., Bernard, J. P., Bersanelli, M., Bielewicz, P., Bock, J. J., Bond, J. R., Borrill, J., Bouchet, F. R., Boulanger, F., Bucher, M., Burigana, C., Butler, R. C., Calabrese, E., Cardoso, J. F., Carron, J., Challinor, A., Chiang, H. C., Chluba, J., Colombo, L. P. L., Combet, C., Contreras, D., Crill, B. P., Cuttaia, F., de Bernardis, P., de Zotti, G., Delabrouille, J., Delouis, J. M., Di Valentino, E., Diego, J. M., Doré, O., Douspis, M., Ducout, A., Dupac, X., Dusini, S., Efstathiou, G., Elsner, F., Enßlin, T. A., Eriksen, H. K., Fantaye, Y., Farhang, M., Fergusson, J., Fernandez-Cobos, R., Finelli, F., Forastieri, F., Frailis, M., Fraisse, A. A., Franceschi, E., Frolov, A., Galeotta, S., Galli, S., Ganga, K., Génova-Santos, R. T., Gerbino, M., Ghosh, T., González-Nuevo, J., Górski, K. M., Gratton, S., Gruppuso, A., Gudmundsson, J. E., Hamann, J., Handley, W., Hansen, F. K., Herranz, D., Hildebrandt, S. R., Hivon, E., Huang, Z., Jaffe, A. H., Jones, W. C., Karakci, A., Keihänen, E., Keskitalo, R., Kiiveri, K., Kim, J., Kisner, T. S., Knox, L., Krachmalnicoff, N., Kunz, M., Kurki-Suonio, H., Lagache, G., Lamarre, J. M., Lasenby, A., Lattanzi, M., Lawrence, C. R., Le Jeune, M., Lemos, P., Lesgourgues, J., Levrier, F., Lewis, A., Liguori, M., Lilje, P. B., Lilley, M., Lindholm, V., López-Caniego, M., Lubin, P. M., Ma, Y. Z., Macías-Pérez, J. F., Maggio, G., Maino, D., Mandolesi, N., Mangilli, A., Marcos-Caballero, A., Maris, M., Martin, P. G., Martinelli, M., Martínez-González, E., Matarrese, S., Mauri, N., McEwen, J. D., Meinhold, P. R., Melchiorri, A., Mennella, A., Migliaccio, M., Millea, M., Mitra, S., Miville-Deschênes, M. A., Molinari, D., Montier, L., Morgante, G., Moss, A., Natoli, P., Nørgaard-Nielsen, H. U., Pagano, L., Paoletti, D., Partridge, B., Patanchon, G., Peiris, H. V., Perrotta, F., Pettorino, V., Piacentini, F., Polastri, L., Polenta, G., Puget, J. L., Rachen, J. P., Reinecke, M., Remazeilles, M., Renzi, A., Rocha, G., Rosset, C., Roudier, G., Rubiño-Martín, J. A., Ruiz-Granados, B., Salvati, L., Sandri, M., Savelainen, M., Scott, D., Shellard, E. P. S., Sirignano, C., Sirri,

G., Spencer, L. D., Sunyaev, R., Suur-Uski, A. S., Tauber, J. A., Tavagnacco, D., Tenti, M., Toffolatti, L., Tomasi, M., Trombetti, T., Valenziano, L., Valiviita, J., Van Tent, B., Vibert, L., Vielva, P., Villa, F., Vittorio, N., Wandelt, B. D., Wehus, I. K., White, M., White, S. D. M., Zacchei, A., Zonca, A., 2020, 'Planck 2018 results. VI. Cosmological parameters', *A&A*, 641, A6.

Riess, A. G., Filippenko, A. V., Challis, P., Clocchiatti, A., Diercks, A., Garnavich, P. M., Gilliland, R. L., Hogan, C. J., Jha, S., Kirshner, R. P., Leibundgut, B., Phillips, M. M., Reiss, D., Schmidt, B. P., Schommer, R. A., Smith, R. C., Spyromilio, J., Stubbs, C., Suntzeff, N. B., Tonry, J., 1998, 'Observational Evidence from Supernovae for an Accelerating Universe and a Cosmological Constant', *The Astronomical Journal*, 116 (3), 1009–1038.

Rosati, P., Borgani, S., Norman, C., 2002, 'The Evolution of X-ray Clusters of Galaxies', *Annual Reviews in Astronomy & Astrophysics*, 40, 539–577.

Rubin, R. H., 1968, 'A Discussion of the Sizes and Excitation of H II Regions', *ApJ*, 154, 391.

Rykoff, E. S., Rozo, E., Hollowood, D., Bermeo-Hernandez, A., Jeltema, T., Mayers, J., Romer, A. K., Rooney, P., Saro, A., Vergara Cervantes, C., Wechsler, R. H., Wilcox, H., Abbott, T. M. C., Abdalla, F. B., Allam, S., Annis, J., Benoit-Lévy, A., Bernstein, G. M., Bertin, E., Brooks, D., Burke, D. L., Capozzi, D., Carnero Rosell, A., Carrasco Kind, M., Castander, F. J., Childress, M., Collins, C. A., Cunha, C. E., D'Andrea, C. B., da Costa, L. N., Davis, T. M., Desai, S., Diehl, H. T., Dietrich, J. P., Doel, P., Evrard, A. E., Finley, D. A., Flaugher, B., Fosalba, P., Frieman, J., Glazebrook, K., Goldstein, D. A., Gruen, D., Gruendl, R. A., Gutierrez, G., Hilton, M., Honscheid, K., Hoyle, B., James, D. J., Kay, S. T., Kuehn, K., Kuropatkin, N., Lahav, O., Lewis, G. F., Lidman, C., Lima, M., Maia, M. A. G., Mann, R. G., Marshall, J. L., Martini, P., Melchior, P.,

Miller, C. J., Miquel, R., Mohr, J. J., Nichol, R. C., Nord, B., Ogando, R., Plazas, A. A., Reil, K., Sahlén, M., Sanchez, E., Santiago, B., Scarpine, V., Schubnell, M., Sevilla-Noarbe, I., Smith, R. C., Soares-Santos, M., Sobreira, F., Stott, J. P., Suchyta, E., Swanson, M. E. C., Tarle, G., Thomas, D., Tucker, D., Uddin, S., Viana, P. T. P., Vikram, V., Walker, A. R., Zhang, Y., DES Collaboration, 2016, 'The RedMaPPer Galaxy Cluster Catalog From DES Science Verification Data', *The Astrophysical Journal Supplement Series*, 224 (1), 1.

Salpeter, E. E., 1955, 'The Luminosity Function and Stellar Evolution.', *ApJ*, 121, 161.

Santos, J. S., Altieri, B., Popesso, P., Strazzullo, V., Valtchanov, I., Berta, S., Böhringer, H., Conversi, L., Demarco, R., Edge, A. C., Lidman, C., Lutz, D., Metcalfe, L., Mullis, C. R., Pintos-Castro, I., Sánchez-Portal, M., Rawle, T. D., Rosati, P., Swinbank, A. M., Tanaka, M., 2013, 'Dust-obscured star formation in the outskirts of XMMU J2235.3-2557, a massive galaxy cluster at z = 1.4', *MNRAS*, 433 (2), 1287–1299.

Sha, F., Lin, Y., Saul, L. K., Lee, D. D., 2007, 'Multiplicative updates for nonnegative quadratic programming', *Neural computation*, 19 (8), 2004—2031.

Springel, V., 2010, 'E pur si muove: Galilean-invariant cosmological hydrodynamical simulations on a moving mesh', *MNRAS*, 401 (2), 791–851.

Springel, V., White, S. D. M., Jenkins, A., Frenk, C. S., Yoshida, N., Gao, L., Navarro, J., Thacker, R., Croton, D., Helly, J., Peacock, J. A., Cole, S., Thomas, P., Couchman, H., Evrard, A., Colberg, J., Pearce, F., 2005, 'Simulations of the formation, evolution and clustering of galaxies and quasars', *nat*, 435 (7042), 629–636.

Stach, S. M., Swinbank, A. M., Smail, I., Hilton, M., Simpson, J. M., Cooke, E. A., 2017, 'ALMA Pinpoints a Strong Overdensity of U/LIRGs in the Massive Cluster XCS J2215 at z = 1.46', *ApJ*, 849 (2), 154.

Stalin, C. S., Petitjean, P., Srianand, R., Fox, A. J., Coppolani, F., Schwope, A., 2010, 'Optical identification of XMM sources in the Canada-France-Hawaii Telescope Legacy Survey', *MNRAS*, 401 (1), 294–306.

Stanford, S., 1997. A Morphological Census of z ¿ 1 Cluster Galaxies in the Optical Rest–frame. HST Proposal ID 7872. Cycle 7.

Stanford, S. A., Romer, A. K., Sabirli, K., Davidson, M., Hilton, M., Viana, P. T. P., Collins, C. A., Kay, S. T., Liddle, A. R., Mann, R. G., Miller, C. J., Nichol, R. C., West, M. J., Conselice, C. J., Spinrad, H., Stern, D., Bundy, K., 2006, 'The XMM Cluster Survey: A Massive Galaxy Cluster at z = 1.45', *The Astrophysical Journal*, 646 (1), L13–L16.

Zwicky, F., 1933, 'Die Rotverschiebung von extragalaktischen Nebeln', *Helvetica Physica Acta*, 6, 110–127.